Direct simulations of low-Reynolds-number turbulent flow in a rotating channel

By REIDAR KRISTOFFERSEN† AND HELGE I. ANDERSSON

Department of Applied Mechanics, Faculty of Mechanical Engineering, The Norwegian Institute of Technology, N-7034 Trondheim, Norway

Direct numerical simulations of fully developed pressure-driven turbulent flow in a rotating channel have been performed. The unsteady Navier–Stokes equations were written for flow in a constantly rotating frame of reference and solved numerically by means of a finite-difference technique on a $128 \times 128 \times 128$ computational mesh. The Reynolds number, based on the bulk mean velocity U_m and the channel half-width h, was about 2900, while the rotation number $Ro = 2|\Omega|h/U_m$ varied from 0 to 0.5. Without system rotation, results of the simulation were in good agreement with the accurate reference simulation of Kim, Moin & Moser (1987) and available experimental data. The simulated flow fields subject to rotation revealed fascinating effects exerted by the Coriolis force on channel flow turbulence. With weak rotation ($Ro = 0.01$) the turbulence statistics across the channel varied only slightly compared with the non-rotating case, and opposite effects were observed near the pressure and suction sides of the channel. With increasing rotation the augmentation and damping of the turbulence along the pressure and suction sides, respectively, became more significant, resulting in highly asymmetric profiles of mean velocity and turbulent Reynolds stresses. In accordance with the experimental observations of Johnston, Halleen & Lezius (1972), the mean velocity profile exhibited an appreciable region with slope 2Ω. At $Ro = 0.50$ the Reynolds stresses vanished in the vicinity of the stabilized side, and the nearly complete suppression of the turbulent agitation was confirmed by marker particle trackings and two-point velocity correlations. Rotational-induced Taylor–Görtler-like counter-rotating streamwise vortices have been identified, and the simulations suggest that the vortices are shifted slightly towards the pressure side with increasing rotation rates, and the number of vortex pairs therefore tend to increase with Ro.

1. Introduction

Turbulent flows in rotating reference frames are of considerable interest in a variety of industrial, geophysical and astrophysical applications. Fluid motions at large scales on a planet as well as the flow in rotating machinery are largely affected by system rotation. The fluid motions are turbulent in the majority of practical cases (e.g. natural flows like ocean currents, estuaries and atmospheric boundary layers, and engineering flows in rotating devices such as turbines, pumps, compressors and cyclone separators), and it is well known that system rotation affects both the mean motion and the turbulence structure. Striking examples of the many fascinating rotational-induced flow phenomena have been reviewed by Tritton (1978, 1985) and Hopfinger (1989). Recent advances in the field are summarized in the report on the Euromech colloquium on the effect of background rotation on fluid motions (Hopfinger & Linden 1990).

† Also: ERCOFTAC Pilot Centre, EPFL-Ecublens, CH-1015 Lausanne, Switzerland.

1.1. *Stability of rotating shear flows*

In laminar and turbulent shear flows subject to system rotation the resulting flow pattern depends on the orientation of the rotation vector with respect to the shear vorticity vector. The effects of rotation on wall-bounded and free shear flows in spanwise rotation, for example, depend on whether the rotation axis is parallel or antiparallel to the shear vorticity. An analogy was drawn by Bradshaw (1969) between shear flows rotating about a spanwise axis, shear layers over curved surfaces (the curvature of the streamlines being in the plane of mean shear), and stratified shear flows in a gravitational field. Although the analogy between the three types of body forces (i.e. Coriolis, centrifugal, and buoyancy) is not so close in turbulence as in laminar flows, many of the spectacular effects exerted on shear flow turbulence by the body forces are analogous.

For an approximately unidirectional shear flow having velocity $U = U(y)$ in the x-direction in a Cartesian reference frame rotating with angular velocity Ω about the z-axis, the ratio of background vorticity 2Ω to mean shear vorticity $-dU/dy$ is

$$S = -2\Omega/(dU/dy). \qquad (1)$$

Thus, the background vorticity and the shear vorticity are of the same sign when $S > 0$ and of opposite signs otherwise. The vorticity ratio defined in (1) is a form of gradient rotation number, or, alternatively, an inverse Rossby number. By drawing a formal algebraic analogy between common meteorological parameters and the parameters describing the effects of system rotation, Bradshaw (1969) defined an equivalent gradient 'Richardson number' as

$$B = S(S+1) \qquad (2)$$

and an equivalent flux 'Richardson number' as $Ri = S/(S+1)$. Tritton (1992) argues that this is a somewhat misleading nomenclature, and alternatively suggests calling B the Bradshaw number.

The role of these dimensionless parameters in rotating flows was first recognized by Bradshaw (1969), and more formally demonstrated by Johnston, Halleen & Lezius (1972) by considering simplified forms of the transport equations for the individual components of the Reynolds stress tensor. A 'displaced particle analysis' (Tritton & Davies 1981; Tritton 1992) led to the same conclusions, although the latter approach is related to the stability of laminar shear flows rather than to turbulence. Nevertheless, both lines of argument led to the same main result, namely that the effect of rotation is *destabilizing* when

$$-1 < S < 0, \quad \text{i.e.} \quad B < 0. \qquad (3)$$

Maximum destabilization occurs for $S = -\frac{1}{2}$ ($B = -\frac{1}{4}$), and restabilization of the flow may be expected when $S < -1$. Positive S, on the other hand, is always associated with stabilized flow. The above criterion for maximum destabilization is supported by the linear spectral analysis of Bertoglio (1982). More recently, Tritton (1992) and Cambon *et al.* (1993) have elaborated on this essential issue.

1.2. *Laminar shear flows in spanwise rotation*

The effects of stabilization and destabilization on laminar shear flows subject to rotation have been demonstrated in a number of papers (see e.g. Tritton & Davies 1981). Since then Koyama *et al.* (1979) and Masuda, Okamae & Ariga (1985) studied the stability of laminar boundary layers in spanwise rotation. Their experimental investigations revealed that the laminar–turbulent transition is suppressed if the

rotation is stabilizing $(S > 0)$, while the critical Reynolds number for transition decreases with increasing destabilizing rotation. However, the transitional boundary-layer flow is qualitatively different in the stabilized and destabilized cases.

The numerical studies by Speziale (1982, 1986) and Speziale & Thangham (1983) of pressure-driven laminar flows in rotating ducts focused mainly on the development of streamwise roll cells due to the Coriolis force instability, which is the rotational analogue of the centrifugal or Taylor instability arising, for instance, in curved channels. The recent flow visualization study by Alfredsson & Persson (1989) demonstrated that the primary instability in rotating Poiseuille flow takes the form of regularly spaced roll cells aligned with the main flow, and the results of the accompanying linear stability analysis are consistent with their experimental findings.

1.3. *Turbulent shear flows in spanwise rotation*

The stability criterion (3) also applies for turbulent shear flows, although the terms 'stabilizing' and 'destabilizing' have a somewhat different meaning in turbulent flow situations. In the following, these words will be used to describe turbulent shear flows whose turbulence intensity is decreased (stabilized) or increased (destabilized) due to system rotation.

The pioneering experimental investigations of rotating turbulent duct flows by Hill & Moon (1962), Moon (1964) and Moore (1967) demonstrated the action of the Coriolis forces on the mean flow and indicated a rotational-induced alteration in the turbulence field. The flow visualizations and more detailed measurements by Johnston *et al.* (1972) and Johnston (1973) revealed that the turbulence level in their rotating water channel is enhanced along the pressure (leading) side where $S < 0$ and correspondingly reduced along the suction (trailing) side of the channel where S is positive. They also observed the development of large-scale Taylor–Görtler-like vortices on the destabilized (pressure) side of the channel, while a nearly total suppression of the turbulence was observed along the stabilized (suction) side. This relaminarization occurred for the lower Reynolds number at relatively high rotation rates. Similar rotational-induced effects on developing turbulent boundary layers were also identified by Koyama *et al.* (1979), Koyama & Ohuci (1985), Watmuff, Witt & Joubert (1985), and Ibal (1990) in their rotating wind tunnels, whereas the combined effects of Coriolis and centrifugal forces were examined experimentally by Kikuyama *et al.* (1987).

Rothe & Johnston (1979) investigated the Coriolis force effects on the developing shear layer downstream of a backward-facing step in a two-dimensional water channel in spanwise rotation, while Witt & Joubert (1985) studied a turbulent wake in a rotating fluid. The structure of a turbulent mixing layer developing in a rotating water channel has been considered more recently by Bidokhti & Tritton (1992). These studies also revealed that free turbulent shear layers are crucially influenced by system rotation.

1.4. *Numerical experiments*

Direct and large-eddy simulations of turbulence, which require the solution of three-dimensional time-dependent momentum equations, may complement experimental investigations of rotating shear flows in a fruitful way, and thereby promote our understanding of the influences of rotation on the turbulence structure. The large-eddy simulations (LES) of fully developed plane Poiseuille flow in a rotating channel by Kim (1983) and Miyake & Kajishima (1986*a, b*) reproduced many of the experimentally observed effects of the Coriolis forces on the mean flow and its turbulence structure. However, the relaminarization (i.e. transition from turbulent to laminar flow) along

the stabilized suction side, as observed experimentally by Johnston *et al.* (1972), was not reproduced in these simulations.

1.5. *Turbulence closure models for rotating flows*

Recent developments in computer systems and efficient calculation algorithms have made three-dimensional viscous flow codes available as engineering design tools, for example in the turbomachinery industry. However, the success of computational analysis of industrial flow phenomena relies heavily on the turbulence model embodied in the computer code. An earlier practice had been to introduce *ad hoc* modifications in Boussinesq-type eddy-viscosity models to account for the rotational effects (see, for instance, Johnston & Eide 1976 and Howard, Patankar & Bordynuik 1980). Today, it is generally accepted that current turbulence models based on the eddy-viscosity hypothesis are unable to capture the important influences of the Coriolis force field on the mean motion and the turbulence field (see, for example, the recent reviews by Launder 1989 *a*, *b*). Unlike the eddy-viscosity models, Coriolis terms associated with system rotation are automatically included in the so-called second-moment closures. More specifically, exact production terms appear as sources (or sinks) in the transport equations for the individual Reynolds stress components, and the resulting second-moment model should therefore be capable of mimicking the complex rotational-induced interplay between the different components of the Reynolds stress tensor.

Some successful applications of second-moment closures to rotating turbulent shear flows have been reported recently. Launder, Tselepidakis & Younis (1987), Kristoffersen, Nilsen & Andersson (1990), and Launder & Tselepidakis (1993) calculated the fully developed flow in a rotating channel, while Nilsen & Andersson (1990 *a*), Galperin & Mellor (1991) and Shima (1993) considered the developing boundary-layer flow in the entrance region of a channel in spanwise rotation. The free shear layer flow developing downstream of a backward-facing step subject to system rotation was calculated by Nilsen & Andersson (1990 *b*) and the rotational effects on the mixing layer downstream of a splitter plate were examined by Nilsen & Andersson (1993).

Rapid distortion theory (RDT) has been adopted by Bertoglio (1982) and Andersson & Mazumdar (1993) in their analysis of homogeneous shear flow subject to system rotation. The linear RDT approach, which neglects triple velocity correlations, retains the pressure–strain interactions which are responsible for the important energy transfer between the spectral components. A somewhat more advanced spectral approach to the modelling and analysis of turbulence subject to system rotation has been advocated by Cambon and his colleagues, see e.g. Cambon, Teissedre & Jeandel (1985) and Cambon & Jacquin (1989). Both linear and nonlinear Coriolis-force effects were predicted by their approach, which is based on a EDQNM (eddy damped quasi-normal Markovian) two-point closure model.

1.6. *Present contribution*

The motivation for the present study is twofold. Firstly, laboratory investigations of turbulence in rotating reference systems are more difficult to accomplish than most other experiments, simply because the flow apparatus has to be mounted on a rotating turntable. Secondly, fully developed flows, in which the mean velocity and the turbulence statistics do not change along the parallel streamlines, are particularly useful in the testing of engineering turbulence models at various levels of closure. However, while fully developed flows are relatively difficult to realize in the laboratory, especially in a rotating system, such flows are attractive objects for direct numerical
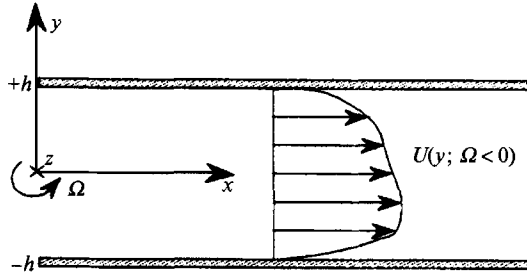
FIGURE 1. Sketch of computational domain and coordinate system.

simulations (DNS). Moreover, system rotation can be accounted for in a direct numerical simulation simply by adding Coriolis force terms into the governing time-dependent momentum equations.

The objective of this investigation is therefore to perform direct numerical simulations of fully developed low-Reynolds-number turbulent channel flow subject to spanwise rotation. The aim is to carry out direct simulations on a fine computational grid for some different rotation numbers. All essential scales of the turbulent motions should be resolved, and the need for a sub-grid-scale (SGS) model, as inherent in the large-eddy simulation approach, is thereby avoided. Moreover, the crucial question of whether the SGS-model should depend on the rotation rate or not (see e.g. Thomas & Takhar 1988), is irrelevant with respect to direct simulations.

The data bases generated will contain three-dimensional velocity and pressure fields for the six different non-zero rotation rates to be considered. The computed results will be compared qualitatively and quantitatively with data and flow visualizations of the rotating channel flow examined by Johnston *et al.* (1972) and Johnston (1973). Data that are practically inaccessible in physical experiments will also be provided. The numerically simulated flow fields may provide further insight into the structure and statistics of wall-bounded turbulent shear flows subject to system rotation, and also be used for design, testing and calibration of closure models designated for rotating turbulent flows.

2. Formulation of the problem

2.1. *Flow configuration and governing equations*

Let us consider the pressure-driven turbulent flow between two infinite parallel plates in spanwise rotation with constant angular velocity $\boldsymbol{\Omega} = (0, 0, \Omega)$ about the z-axis in a Cartesian coordinate system, as shown schematically in figure 1. The governing Navier–Stokes equations for time-dependent motion of an incompressible flow in a reference frame rotating with the plates can be expressed in the following dimensionless form:

$$\boldsymbol{\nabla} \cdot \boldsymbol{u} = 0, \tag{4}$$

$$\frac{\partial \boldsymbol{u}}{\partial t} + (\boldsymbol{u} \cdot \boldsymbol{\nabla}) \boldsymbol{u} = -\boldsymbol{\nabla} p_{eff} + \frac{1}{Re_\tau} \nabla^2 \boldsymbol{u} - Ro_\tau \frac{\boldsymbol{\Omega}}{\Omega} \times \boldsymbol{u}. \tag{5}$$

Here, the variables have been non-dimensionalized by h and u_τ, where $2h$ denotes the distance between the parallel plates and u_τ is a velocity scale to be defined later. The two independent dimensionless parameters inherent in the flow problem are the rotation number

$$Ro_\tau = 2\Omega h / u_\tau \tag{6a}$$

and the Reynolds number

$$Re_\tau = u_\tau h/\nu,\tag{6b}$$

where ν is the kinematic viscosity of the fluid.

The final term in the momentum equation (5) represents the Coriolis force due to system rotation, while the centrifugal force term also associated with the rotation of the reference frame has been absorbed in the effective pressure

$$p_{eff} = p - \tfrac{1}{8}Ro_\tau^2 r^2,\tag{7}$$

where p is the normalized static pressure and r denotes the dimensionless distance from the axis of rotation. According to engineering practice, the instantaneous flow field (u, p_{eff}) governed by (4) and (5) can conveniently be split into mean (U, P_{eff}) and fluctuating (u', p'_{eff}) parts. This decomposition will be adopted in the analysis of the simulated channel flow data.

2.2 Streamwise force balance and scaling velocities

The fully developed flow under consideration is driven by an imposed mean pressure gradient

$$\frac{\mathrm{d}P_{eff}}{\mathrm{d}x} = -1\tag{8}$$

in the x-direction, so that the turbulence may be treated as homogeneous in the streamwise (x) and spanwise (z) directions, i.e. mean properties and turbulence statistics vary only in the y-direction normal to the plates. By prescribing the dimensionless driving force according to (8), the velocity scale u_τ is implicitly defined in terms of the square root of the dimensional mean pressure gradient $\mathrm{d}P^*_{eff}/\mathrm{d}x^*$ as follows:

$$u_\tau \equiv \left(-\frac{h}{\rho}\frac{\mathrm{d}P^*_{eff}}{\mathrm{d}x^*}\right)^{\frac{1}{2}},\tag{9}$$

where ρ is the fluid density and the asterisk identifies dimensional quantities.

The resulting unidirectional mean flow, $U = U(y)$ and $V = W = 0$, is governed by the Reynolds-averaged Navier–Stokes equations (RANS), which can readily be derived from the instantaneous equations (4) and (5). By integrating the streamwise mean momentum equation once with respect to y, we obtain

$$-\overline{uv} + Re_\tau^{-1}\frac{\mathrm{d}U}{\mathrm{d}y} = -y - \left[1 - \frac{u_{\tau s}^2}{u_\tau^2}\right],\tag{10}$$

where $u_{\tau s}$ denotes the *local* friction velocity at the plate at $y = -1$, i.e.

$$u_{\tau s}^2 \equiv u_\tau^2\, Re_\tau^{-1}\frac{\mathrm{d}U}{\mathrm{d}y}\bigg|_{y=-1}.\tag{11a}$$

The overbar identifies averages of fluctuating quantities, and the primes are omitted in order to simplify the notation. Correspondingly, $u_{\tau p}$ is the local friction velocity based on the wall shear stress at $y = +1$, i.e.

$$u_{\tau p}^2 \equiv -u_\tau^2\, Re_\tau^{-1}\frac{\mathrm{d}U}{\mathrm{d}y}\bigg|_{y=+1}.\tag{11b}$$

Author(s)	Re	Re_τ	Ro	Ro_τ	Domain in $2h$-units	Grid points
Kim (1983)	13800*	640	0.068*†	1.47	$\pi \times 1.0 \times 0.5\pi$	$68 \times 68 \times 128$
Miyake & Kajishima (1986)	4950	250	0.165	3.0	$4.8 \times 1.0 \times 1.2$	$32 \times 32 \times 32$
Present	2900	194	0.5	7.5	$2\pi \times 1.0 \times \pi$	$128 \times 128 \times 128$
Kim *et al.* (1987)	3300*	180	0	0	$2\pi \times 1.0 \times \pi$	$192 \times 129 \times 160$
Moser & Moin (1987)	2990*	168	Curved channel		$2\pi \times 1.0 \times \frac{2}{3}\pi$	$128 \times 64 \times 128$

* Based on centreline velocity U_c.
† Flow visualizations also for $Ro = 0.21$.

TABLE 1. Characteristics of relevant direct and large-eddy simulations

Combining (11*b*) and (10) for $y = +1$ yields

$$u_\tau^2 = \tfrac{1}{2}(u_{\tau s}^2 + u_{\tau p}^2) \tag{12}$$

which suggests that the scaling velocity u_τ can be interpreted as a *global* wall friction velocity. Furthermore, without system rotation ($\Omega = 0$) the mean flow is symmetric with respect to the (x, z)-plane at $y = 0$ and $u_\tau = u_{\tau s} = u_{\tau p}$.

Throughout the paper the global wall friction velocity u_τ will be used to normalize the flow variables when variations across the entire channel $-1 \leqslant y \leqslant +1$ are presented, while the local friction velocities $u_{\tau s}$ and $u_{\tau p}$ are used in the scaling of computed results whenever the inner coordinate y^+:

$$y^+ \equiv (1+y)u_{\tau s}/\nu \quad (y < 0), \tag{13a}$$

$$y^+ \equiv (1-y)u_{\tau p}/\nu \quad (y > 0), \tag{13b}$$

labels the abscissa.

3. Computational procedure and validation

3.1. *Numerical method*

The simulation code used to numerically solve the governing equations (4) and (5) was an adapted version of ECCLES (explicit channel code for large eddy simulation) developed by Gavrilakis *et al.* (1986). The ECCLES-code, originally intended for large-eddy simulations of turbulent flow fields, has optional subgrid-scale models implemented to account for the dissipation associated with the unresolved small-scale turbulence. Here, however, the code was run without any SGS model.

ECCLES is a finite difference code with staggered positioning of the dependent variables in the computational grid. The spatial derivatives are approximated by second-order-accurate central-difference approximations. A second-order explicit Adams–Bashforth scheme is used for the time derivatives in combination with a split-step technique which leaves a Poisson equation for the pressure field. The use of periodic (i.e. cyclic) boundary conditions in the homogeneous streamwise (x) and spanwise (z) directions allows efficient direct methods for solving the Poisson equation. More specifically, fast Fourier transforms were used in the homogeneous directions, while Gauss elimination and back-substitution were applied in the inhomogeneous y-direction. Gavrilakis *et al.* (1986) should be consulted for further details about the numerical scheme.

3.2. *Computational domain*

The computational domain was of exactly the same size as that used by Kim, Moin
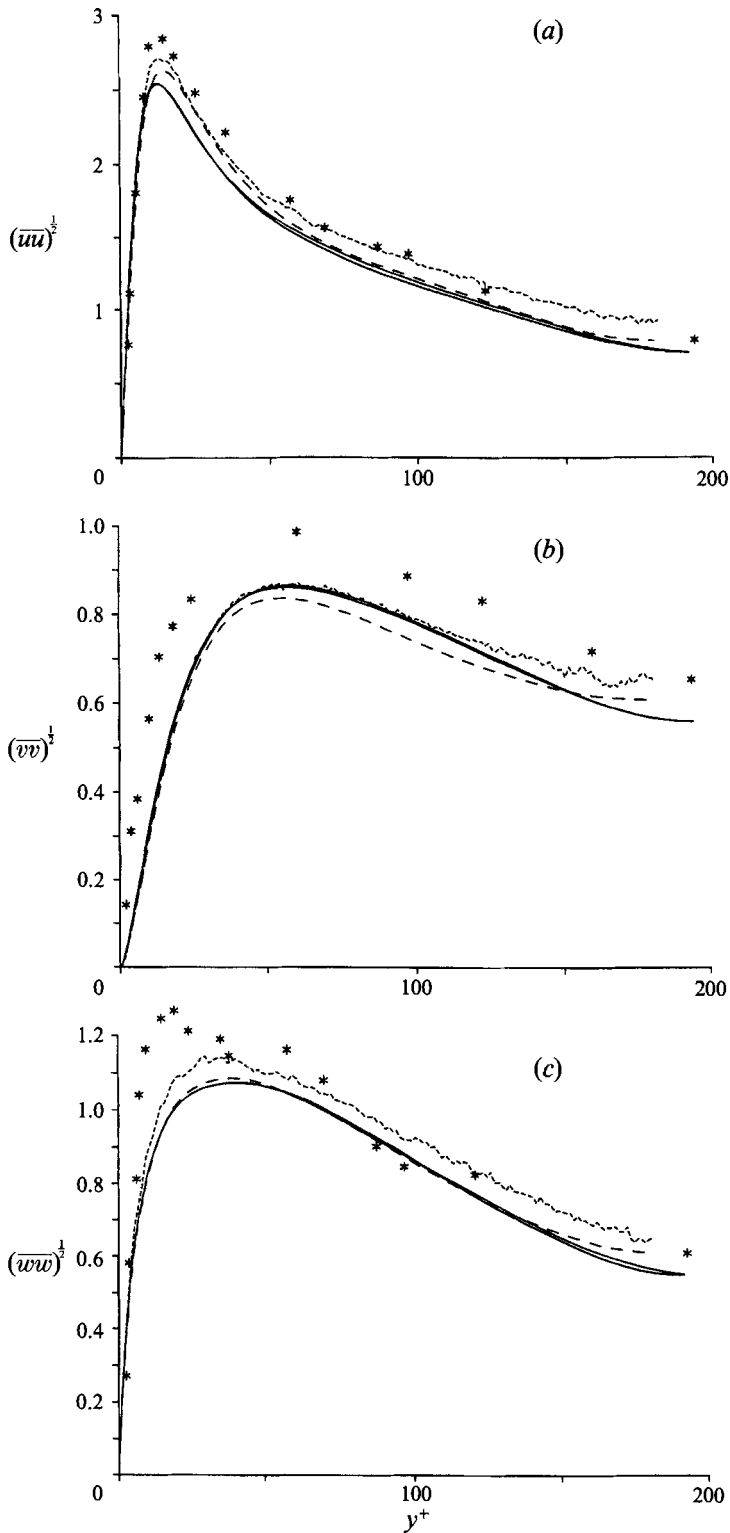
FIGURE 2. For caption see facing page.

& Moser (1987) in their highly accurate simulation of non-rotating channel flow at $Re_\tau = 180$. With lengths $4\pi h$ and $2\pi h$ in the streamwise (x) and spanwise (z) directions, respectively, they verified that the turbulence fluctuations became decorrelated at a separation of one half-period in the streamwise direction. This computational domain is also substantially larger than in any previous numerical simulation of rotating channel flow (see table 1 for an overview). The computational domain was divided into $128 \times 128 \times 128$ nodes, which according to Kim *et al.* (1987) are sufficient to resolve all essential scales of the low-Reynolds-number turbulence.

Some earlier simulations of turbulent channel flows (Deardorff 1970; Schumann 1975) imposed synthetic boundary conditions in the log-layer along the walls. Here, as in the direct simulation of Kim *et al.* (1987), the physical no-slip condition is imposed at the walls and the flow in the near-wall region is explicitly computed. In order to adequately resolve the turbulence scales in the vicinity of the walls, a non-uniform tanh-distribution of the grid points was used in the normal (y) direction. Thus, for the Reynolds number $Re_\tau = 194$ considered here the grid point next to the wall is at $y^+ \approx 0.5$, while the largest spacing is about $\Delta y^+ \approx 5$. For comparison, the equally distributed grid points in the two homogeneous directions yield constant grid spacings $\Delta x^+ \approx 20$ and $\Delta z^+ \approx 10$ in the streamwise and spanwise directions, respectively.

3.3. *Sampling procedure*

Starting from a randomly generated three-dimensional initial field without any physical realism, a numerical transition to physically realistic turbulence took place as the simulation evolved in time (see Kristoffersen & Andersson 1991). Statistically steady turbulence was established when the distribution of the total (viscous plus turbulent) shear stress across the channel became linear, i.e. in accordance with (10). However, in order to ensure an adequate ensemble of statistically independent samples, the simulation had to be continued for several letots. Here, a *letot* (large eddy turn over time) is a characteristic timescale for the motion of the larger eddies, which in our scheme is the time unit h/u_τ already used in the normalization of the governing equations (4) and (5). As system rotation was imposed (or increased) a similar procedure was adopted. Starting from a dump of a previous flow field, the simulation proceeded through a statistically transient stage until a new statistically steady state was reached, followed by a sampling period over which time-averaged data were collected. The computed statistics, denoted by an overbar, are averaged in time as well as over the homogeneous (x, z)-planes. Some aspects of the statistical sampling are discussed by Andersson & Kristoffersen (1992).

3.4. *Validation for non-rotating channel flow*

Direct and large-eddy simulations of plane Poiseuille flow have been performed by Deardorff (1970), Schumann (1975), Moin & Kim (1982), Gavrilakis *et al.* (1986), Kim *et al.* (1987), and many others. The direct simulation of Kim *et al.* is regarded as highly accurate due to their fine grid resolution (twice as many nodes as in the present simulations), and has now become a widely used reference solution for experimentalists and turbulence modellers. Before the results of the simulations of rotating channel flow are presented in §4, it is interesting to compare some primary statistics obtained in the non-rotating case ($Re_\tau = 194$) with the DNS data of Kim *et al.* (1987) for $Re_\tau = 180$.

FIGURE 2. Normalized root-mean-square velocity fluctuations. Both sides are shown for the present simulation. (a) $(\overline{u^2})^{\frac{1}{2}}$; (b) $(\overline{v^2})^{\frac{1}{2}}$; (c) $(\overline{w^2})^{\frac{1}{2}}$; *, Kreplin & Eckelmann (1979); -----, Nishino & Kasagi (1989); ————, Kim *et al.* (1987).

Authors	Technique	u_{rms}/U	w_{rms}/U
Alfredsson et al. (1988)	Hot film	0.40	—
Karlsson (1993)	LDV	0.40	0.18
Kim et al. (1987)	DNS	0.36	0.19
Kreplin & Eckelmann (1979)	Hot film	0.25	0.065
Nishino & Kasagi (1989)	PTV	0.45	0.18
Present	DNS	0.41	0.20

TABLE 2. Measurements of near-wall fluctuations without rotation

Comparisons will also be made with the hot-film measurements of Kreplin & Eckelmann (1979) and the more reliable particle-tracking velocimetry (PTV) data of Nishino & Kasagi (1989) at Re_τ equal to 194 and 205, respectively. The former data were also used as the experimental reference by Kim et al.

First, the dimensional bulk mean velocity U_m can be computed from the dimensionless mean velocity profile $U(y)$ according to its definition

$$U_m \equiv \tfrac{1}{2}u_\tau \int_{-1}^{+1} U\,\mathrm{d}y. \tag{14}$$

The present simulation gives $U_m = 15.1u_\tau$, which corresponds to a bulk Reynolds number

$$Re \equiv U_m h/\nu = Re_\tau U_m/u_\tau, \tag{15}$$

equal to 2900. The ratio of centreline velocity U_c to bulk mean velocity U_m was 1.16, which is in accordance with the experimental correlation $U_c/U_m = 1.28 Re^{-0.0116} = 1.16$ suggested by Dean (1978). The corresponding results of the simulation by Kim et al. (1987) were $U_m/u_\tau = 15.6$ and $U_c/U_m = 1.16$.

The computed turbulence intensities, i.e. the square root of the normal Reynolds stress components, are shown in figure 2. The agreement between the present simulation, the DNS of Kim et al. (1987) and the PTV-data of Nishino & Kasagi (1989) is very good, while the hot-film data of Kreplin & Eckelmann (1979) indicate a somewhat higher turbulence level. The limiting behaviour of the streamwise and spanwise intensities at the wall has been estimated by many experimentalists using different measuring techniques. The data in table 2 are fairly consistent, except for those reported by Kreplin & Eckelmann (1979). However, due to the difficulties associated with hot-film and hot-wire sensors in the viscous sub-layer, Alfredsson et al. (1988) conjectured that the peak values $u_{rms}/U = 0.38$ and $w_{rms} = 0.195$ reported by Kreplin & Eckelmann are better estimates of the asymptotic near-wall behaviour than those in table 2.

The only non-vanishing Reynolds shear stress component $-\overline{uv}$ is shown in figure 3(a) in global coordinates, and in figure 3(b) in wall coordinates. The total kinematic shear stress $-\overline{uv} + Re_\tau^{-1}\,\mathrm{d}U/\mathrm{d}y$ is drawn as a dashed line in figure 3(a), and the slight deviation from the dash-dotted line $-y$, i.e. $u_{\tau s} = u_{\tau p}$ in (10), indicates that the averaging period (9.1 letots) is not fully satisfactory. Nevertheless, the present sampling time compares favourably with the sampling period in other direct simulations. In their plane channel flow simulations, for instance, Gavrilakis et al. (1986) sampled over 3 letots, while Moser & Moin (1987) in their curved channel simulation computed statistics over $6h/u_\tau$. Kim et al. (1987) ran their simulation for about 10 non-dimensional time units (h/u_τ) altogether, but the actual sampling time has not been reported explicitly. The near-wall variation in figure 3(b) shows that the shear stress is
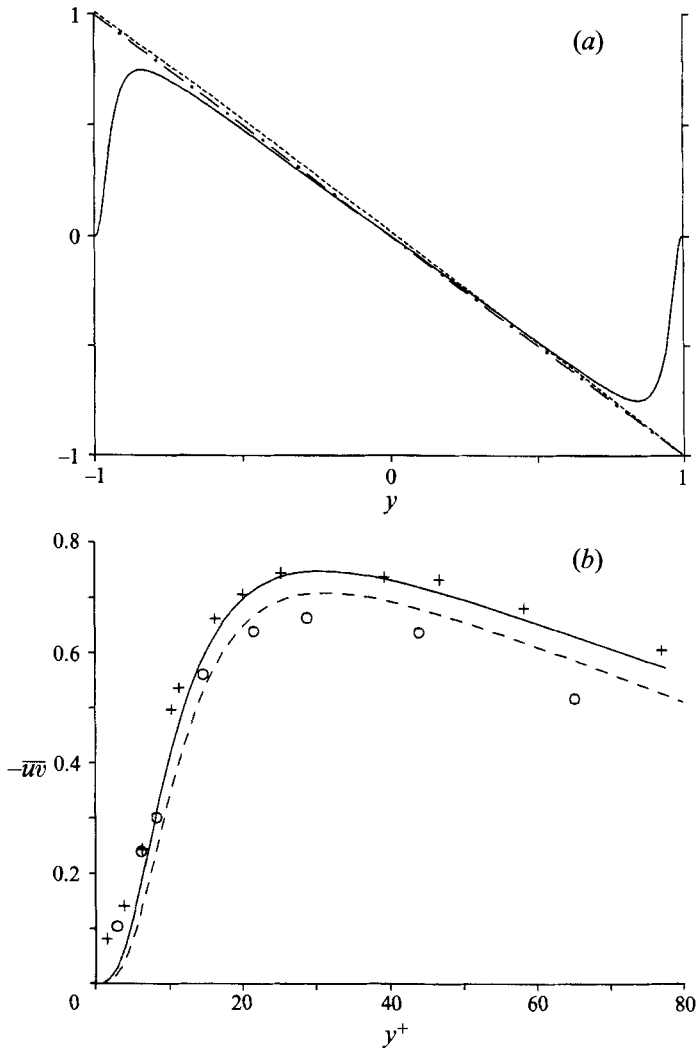
FIGURE 3. Distribution of shear stresses. (*a*) In global coordinates: ———, $-\overline{uv}$; -----, $-\overline{uv} + Re_\tau^{-1}\, \mathrm{d}U/\mathrm{d}y$; —·—·—, $-y$; (*b*) Reynolds shear stress in wall coordinates: ———, $-\overline{uv}$; ◯, Eckelmann (1974), $Re_\tau = 142$; +, Eckelmann, $Re_\tau = 208$; ———, Kim *et al.* (1987).

slightly higher in the present simulation than in that of Kim *et al.*, and this may partly be ascribed to the Reynolds-number effect observed, for example, in the experimental data of Eckelmann (1974). Further comparisons of the computed statistics with the most recent and accurate laboratory measurements, i.e. the PTV-data of Nishino & Kasagi (1989) and the LDV-measurements of Karlsson & Johansson (1988), are provided in Andersson & Kristoffersen (1992). As long as the higher-order moments were compared directly, rather than in terms of the dispersion indices (skewness and flatness), it was concluded that the accuracy of the statistics of the numerically generated channel flow is within the differences between the experimental data sets.

3.5. *Computational details*

The computer simulations were carried out on a CRAY X-MP/28 at NTH in

Trondheim (Norway) and on the CRAY-2 at EPFL in Lausanne (Switzerland). The computations required about 20 Mwords of memory to avoid data transfer to discs during execution, and the main part of the simulations were thus run on the CRAY-2. The performance of 4.5 s per time-step reflects the high degree of vectorization of the code. Nevertheless, the total amount of computer time for the simulations to be reported herein was about 200 CPU hours, corresponding to approximately 100 time units h/u_τ (letot). Thus, one letot required about two CPU-hours of computing time. To keep the costs of the simulations at a reasonable level, the length of the sampling periods was not always fully adequate, and some of the statistical results to be provided in the following sections may suffer somewhat from this.

4. Results and discussion

Starting from an instantaneous field of the non-rotating channel flow simulation described in §3.4, the angular velocity Ω was now set to a non-zero value and the flow field advanced further in time. Statistics were then computed after the flow field had settled at a new statistically steady state. This procedure was repeated for different rotation rates to cover rotation numbers Ro_τ in the range from 0.15 to 7.5. However, when the results are being presented and discussed in the following a rotation number based on the bulk mean velocity U_m defined in (14) is more commonly used, i.e.

$$Ro \equiv 2\,|\Omega|\,h/U_m = |Ro_\tau|\,u_\tau/U_m. \tag{16}$$

It should be emphasized that the channel is rotated with a *negative* angular velocity ($\Omega < 0$) about the z-axis, see figure 1. Accordingly, $Ro_\tau < 0$ whereas $Ro > 0$. Moreover, the two channel walls at $y = -1$ and $y = +1$ become the suction and pressure sides, respectively. Some characteristics of the six different rotating flow simulations are provided in table 3, while the time history of the simulations is presented in figure 4.

4.1. *Mean statistics*

The computed mean velocity profiles are shown in figure 5. While the profile is symmetric about the channel mid-plane $y = 0$ without rotation, the profiles become increasingly asymmetric as the rotation rate increases. Over a certain region the profiles become approximately linear with slope 2Ω, and the width of this region increases with Ro. Since the mean shear vorticity $-dU/dy$ tends to -2Ω, the absolute mean vorticity $2\Omega - dU/dy$ becomes approximately zero. According to the stability criterion in §1.1, this particular portion of the profile represents a region of neutral stability ($S = -1$). These findings are fully consistent with the laboratory measurements of Johnston *et al.* (1972). Tritton (1978), guided by their data, presumed 'a tendency for the turbulence to generate such zones'. It is therefore interesting to recall that the same tendency has been observed in fully developed turbulent flows with streamline curvature. A large portion of irrotational flow, i.e. zero absolute vorticity, has been observed in a curved channel by Wattendorf (1935), between rotating concentric cylinders by Taylor (1935), and in the turbulent boundary layer around a rotating cylinder by Kasagi & Hirata (1975).

The mean velocity profiles are also presented in law-of-the-wall coordinates in figure 5(b), where the inner variables U^+ and y^+ are based on the local friction velocities defined in (11). The difference between the suction and pressure sides is striking, whereas the profiles for $Ro = 0$ are in agreement with the semi-logarithmic law $U^+ = 2.5 \ln y^+ + 5.5$ for y^+ greater than 30. The mean velocity on the suction side lies
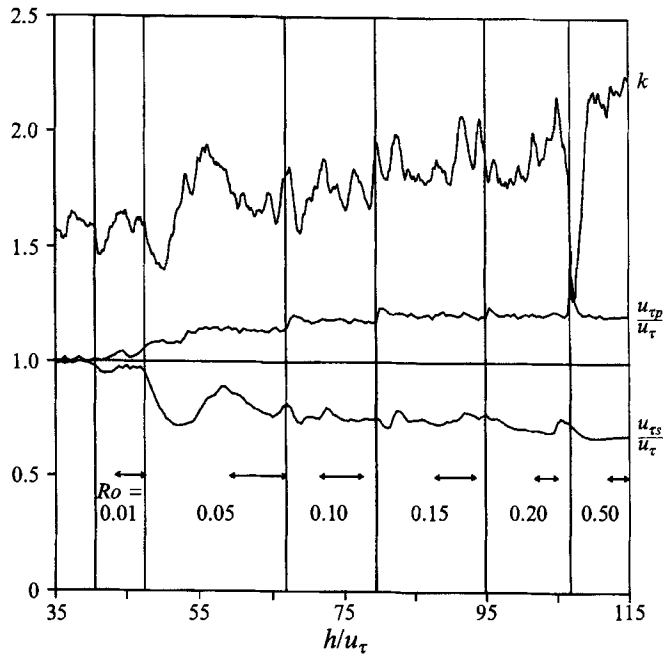
FIGURE 4. Volume-averaged turbulent kinetic energy k and local wall friction velocities $u_{\tau p}/u_\tau$ and $u_{\tau s}/u_\tau$ versus time in letots (h/u_τ). The vertical lines separate the different rotation rates and the sampling periods are indicated by arrows.

Ro	Averaging period in letots (h/u_τ)	$\dfrac{U_m}{u_\tau}$	$\dfrac{u_{\tau p}}{u_\tau}$	$\dfrac{u_{\tau s}}{u_\tau}$	$\left(\dfrac{u_{\tau s}}{u_\tau}\right)^2 + \left(\dfrac{u_{\tau p}}{u_\tau}\right)^2$
0	9.1	15.06	1.002	1.004	2.013
0.01	4.0	15.03	1.023	0.970	1.989
0.05	7.6	15.57	1.140	0.805	1.948
0.10	6.0	15.60	1.185	0.760	1.982
0.15	5.6	15.41	1.213	0.754	2.040
0.20	3.2	15.23	1.217	0.707	1.982
0.50	2.8	15.25	1.207	0.679	1.918

TABLE 3. Simulations for different rotation numbers

above the profile for the non-rotating case. The profile for $Ro = 0.01$ still exhibits a logarithmic region, whereas the profiles for higher Ro have a more laminar-like shape and approach the linear law $U^+ = y^+$. This is in keeping with the measured profiles of Johnston (1973) at his lowest Reynolds number $(Re = 5750)$. Correspondingly, the mean velocity profiles on the pressure side lie below the profile for $Ro = 0$. These profiles exhibit the characteristic turbulent semi-logarithmic shape, but with a slope which decreases as Ro is increased. At the highest rotation rate $(Ro = 0.50)$, however, an anomalous behaviour is observed and the profile diverges from the linear sublayer law at $y^+ \approx 5$. The effects of rotation, as observed from figure 5(b), are in accordance with the stability criterion based on the Bradshaw number B in (2). Obviously dU/dy has opposite signs on the two sides. On the suction side the flow is stabilized since the local vorticity ratio S is positive and $B > 0$, whereas the negative S $(0 > S > -1)$ on
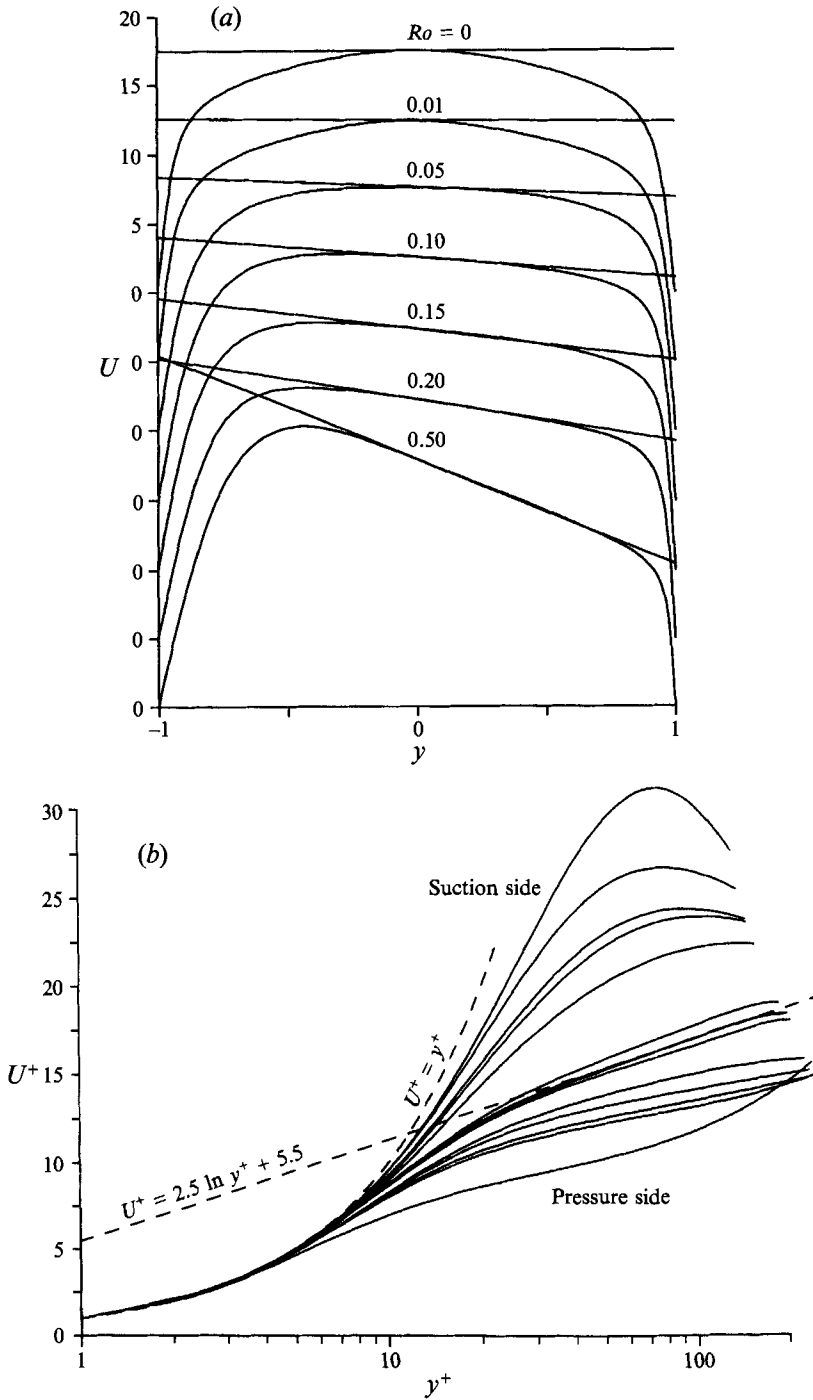
FIGURE 5. Mean velocity profiles for the different rotation rates. (a) In global coordinates, the straight lines have slopes $2\,\Omega$; (b) in wall coordinates.
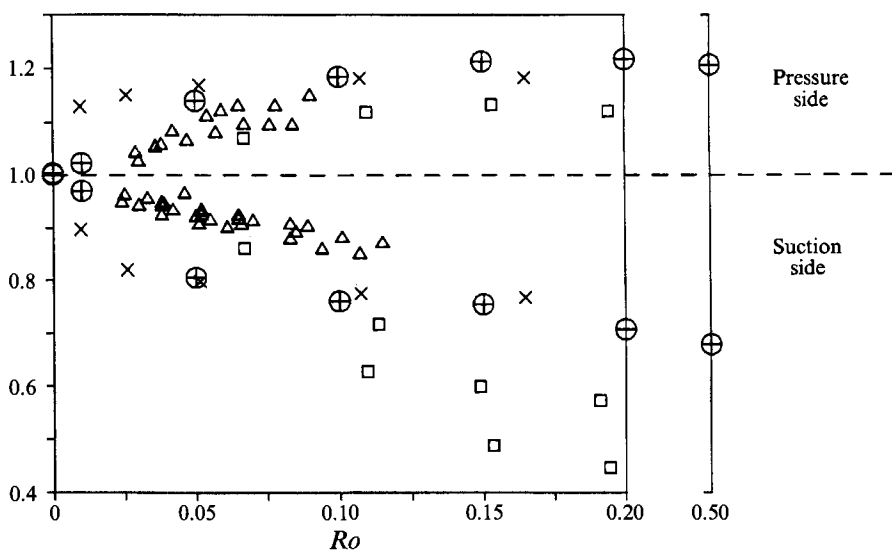
FIGURE 6. Time averaged local wall friction velocities $u_{\tau p}/u_\tau$ and $u_{\tau s}/u_\tau$ as function of Ro: $\oplus$, present DNS; $\square$, experiments by Johnston *et al.* (1972), $Re \approx 5500$; $\triangle$, Johnston *et al.* $11700 < Re < 18000$; $\times$, LES by Miyake & Kajishima (1986a, b).

the pressure side makes $B < 0$ and rotation therefore tends to be destabilizing. It is also interesting to notice that the differences between the suction and pressure side profiles for $Ro = 0.01$ are analogous with the mean velocity profiles on the convex (stable) and concave (unstable) sides of the weakly curved channel flow simulation by Moser & Moin (1987).

Local friction velocities, as defined in (11), are shown as a function of the rotation number in figure 6. The present data are time-averaged values, some of which are quite sensitive to the actual sampling period. The time histories presented in figure 4 indicate that $u_{\tau s}$ is more susceptible to marginal sampling than $u_{\tau p}$, particularly for $Ro = 0.05$. (A better estimate for $u_{\tau s}$ at $Ro = 0.05$ may perhaps be obtained from (12), i.e. $u_{\tau s} = 0.837$.) Nevertheless, the wall friction velocities satisfy (12), which ensures a global mean momentum balance, to within 3 %, except for the highest rotation rate $Ro = 0.50$ (see table 3). The DNS results in figure 6 follow the same trend as the Preston-tube data of Johnston *et al.* (1972) up to $Ro \approx 0.10$, namely that the wall friction is reduced on the suction side and increased on the pressure side due to stabilization and destabilization, respectively. The computed data show, however, an appreciably greater effect of rotation than the experiments. This can partly be ascribed to the definition of Ro adopted by Johnston *et al.* (1972). Their rotation number Ro was defined in terms of Q/A rather than U_m as in (16), i.e. the averaged mean velocity over the rectangular cross-section A, where Q denotes the flow rate. Owing to sidewall effects Q/A is necessarily below U_m at the channel mid-section. Their rotation number Ro is thus slightly overestimated, as compared with the present definition (16), and the experimental data points in figure 6 should therefore have been shifted slightly to the left.

No clearly identifiable Reynolds number effect could be seen in the Preston-tube data of Johnston *et al.* (1972). However, the direct simulations were at a significantly lower Reynolds number (2900) than the range $11700 < Re < 18000$ covered by the experiments. In a recent computational study with a second-moment closure, Launder & Tselepidakis (1993) observed a marked reduction in the difference between $u_{\tau p}$ and
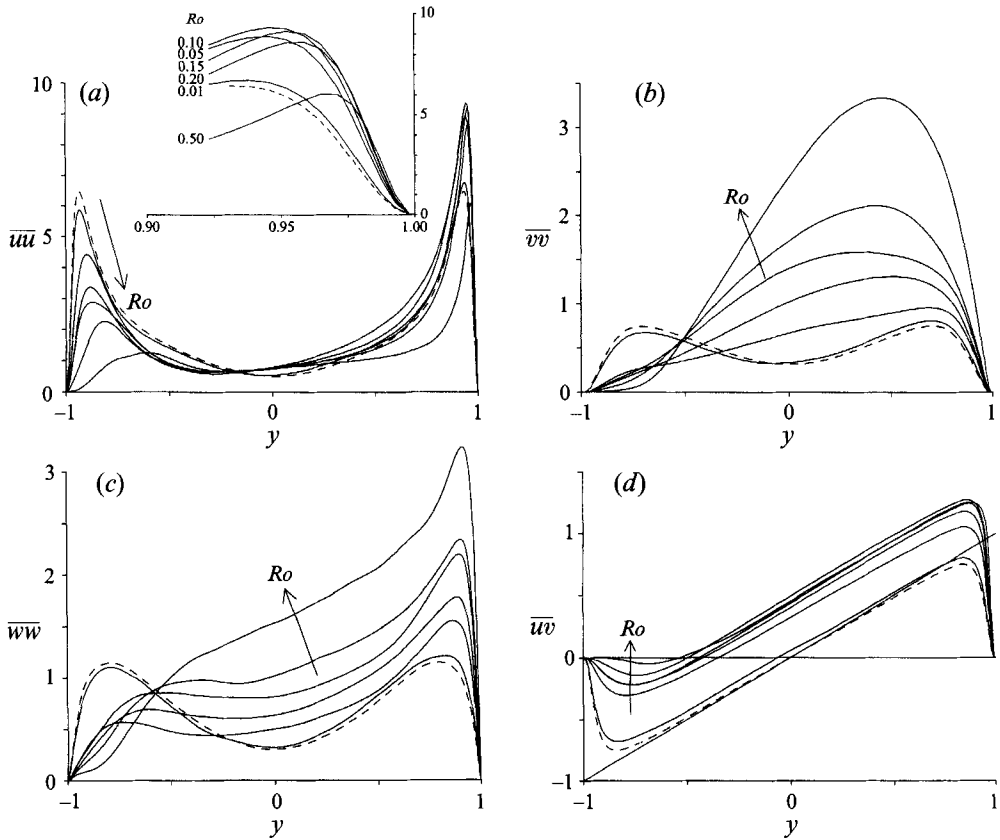
FIGURE 7. Reynolds stress components in global coordinates. (a) $\overline{u^2}$; (b) $\overline{v^2}$; (c) $\overline{w^2}$; (d) $\overline{uv}$. The broken lines represent the non-rotating case.

$u_{\tau s}$ for $Ro = 0.015$ as the Reynolds number was raised from 3100 to 6875. This observation gives some support to the possible existence of a Reynolds-number dependence at low Re.

Some wall friction data at moderate Reynolds numbers ($Re \approx 5500$) were also provided by Johnston et al. (1972) up to $Ro \approx 0.20$. However, the uncertainty level on these results was considered as 'fairly high', since the data were deduced from measured mean velocity profiles by means of the logarithmic law of the wall or the profile slope itself. At the higher rotation rates ($Ro \gtrsim 0.10$) two striking phenomena were observed. The apparent levelling off of the wall friction on the pressure side was reproduced by the DNS all the way up to $Ro = 0.50$, although at a somewhat higher saturation level. On the suction side the rapid drop of the experimental $u_{\tau s}$ data has been ascribed to a transition from turbulent to laminar flow. No such collapse in the suction-side wall friction was observed in the simulations, in spite of the low Reynolds number. Since the driving pressure gradient is kept constant for all Ro considered in the simulations, the wall shear stresses on the two surfaces inevitably have to adjust so as to satisfy the global streamwise momentum balance (12). This constraint is clearly at variance with the experimental conditions and explains the striking differences on the suction side.

Large-eddy simulation data of Miyake & Kajishima (1986a, b) are also plotted in figure 6. In spite of their coarse grid (see table 1) and the modelling of the small-scale

ij	11	22	33	12
P_{ij}	$-2\overline{uv}\,\mathrm{d}U/\mathrm{d}y$	0	0	$-\overline{v^2}\,\mathrm{d}U/\mathrm{d}y$
G_{ij}	$4\Omega\,\overline{uv}$	$-4\Omega\,\overline{uv}$	0	$-2\Omega(\overline{u^2}-\overline{v^2})$

TABLE 4. Production terms due to mean shear (P) and rotation (G) for unidirectional flow $U = U(y)$

stresses, the LES results are in excellent agreement with our DNS data for $Ro \geqslant 0.05$. For lower rotation rates, on the other hand, the LES results exhibit a greater response to rotation than suggested by the experimental data and the DNS.

The non-zero Reynolds stress components $\overline{u^2}$, $\overline{v^2}$, $\overline{w^2}$ and $\overline{uv}$, normalized by the global wall friction velocity (9), are shown in figure 7 for different rotation numbers. The overall tendency, albeit with some exceptions, is that the Reynolds stresses are reduced on the suction side and increased on the pressure side due to the imposed system rotation. The action of the Coriolis forces at $Ro = 0.01$ can be considered as a perturbation to the non-rotating case, whereas strong and asymmetric changes are observed for $Ro \geqslant 0.05$.

Considerations of how rotation affects the Reynolds stress components can be based on transport equations for the individual stress components. These equations, generalized to include system rotation, are given by Launder *et al.* (1987), and in simplified form by Johnston *et al.* (1972). Here, attention is focused on the production terms

$$P_{ij} = -\left[\overline{u_i u_k}\frac{\partial U_j}{\partial x_k} + \overline{u_j u_k}\frac{\partial U_i}{\partial x_k}\right], \tag{17}$$

$$G_{ij} = -2\Omega_k\left[\overline{u_j u_m}\,\epsilon_{ikm} + \overline{u_i u_m}\,\epsilon_{jkm}\right] \tag{18}$$

associated with mean shear and rotational stress generation, respectively. To facilitate the interpretation of the results in figure 7, P_{ij} and G_{ij} are written in component form in table 4 for fully developed two-dimensional channel flow. It may be worthwhile to recall that in the non-rotating case $\overline{uv}$ is of opposite sign to $\mathrm{d}U/\mathrm{d}y$, where $\mathrm{d}U/\mathrm{d}y$ is positive for $y < 0$ and vice versa. This makes $P_{11} > 0$ across the entire channel, whereas P_{12} attains the same sign as y. Since $P_{22} = P_{33} = 0$ there is no direct production of either $\overline{v^2}$ or $\overline{w^2}$, but energy is transferred into these components by pressure–strain interactions.

The direct effects of (negative) system rotation are expected to reduce $\overline{v^2}$ and increase $\overline{u^2}$ on the *suction* side of the channel since $G_{22} = -G_{11} < 0$, whereas $G_{12} > 0$ tends to reduce the negative level of $\overline{uv}$. The fluctuations normal to the wall (figure 7b) are indeed damped considerably in the vicinity of the wall, and the characteristic near-wall peak tends to disappear even for $Ro = 0.05$. The magnitude of the mean shear production P_{12} reduces with decreasing $\overline{v^2}$, and this indirect effect of rotation accompanies the direct production G_{12} in the damping of $\overline{uv}$ observed in figure 7(d). Contrary to the expected behaviour, however, the streamwise component $\overline{u^2}$ in figure 7(a) decreases monotonically with Ro. This suggests that alterations in the total production $P_{11} + G_{11} = (1 + S)P_{11}$ are dominated by the indirect reduction of the mean shear production P_{11} due to the reduced shear stress level. Inspection of the ratio G_{11}/P_{11}, which can be identified as the vorticity ratio S defined in (1), does indeed show that S attains positive values appreciably below unity near the suction side. Although $P_{33} = G_{33} = 0$, the profiles of $\overline{w^2}$ in figure 7(c) show that the normal stress in the spanwise direction is significantly affected by rotation. Since $\overline{u^2}$ and $\overline{v^2}$ are reduced due

to rotation on the suction side, less energy becomes available for redistribution into $\overline{w^2}$ by pressure–strain processes. It is conjectured that this is the major cause of the observed reduction in $\overline{w^2}$, although rotation of the reference frame is known also to affect the instantaneous pressure field, and thus the pressure–strain interactions, directly (see, for instance, Cousteix & Aupoix 1981; Bertoglio 1982 and Kristoffersen *et al.* 1990). Another noticeable feature exhibited by the results presented in figure 7 is that the characteristic near-wall peaks of $\overline{u^2}$, $\overline{w^2}$ and $\overline{uv}$ are shifted away from the suction side towards the centre of the channel, a tendency which can partly be ascribed to the increasing lengthscale $v/u_{\tau s}$ associated with increasing rotation rates.

Near the *pressure* side the turbulence level is augmented by weak and moderate rotation. The rotational stress generation terms, $G_{22} = -G_{11} > 0$ and $G_{12} > 0$, tend to increase $\overline{v^2}$ and $\overline{uv}$, and to reduce $\overline{u^2}$. The mean shear production P_{11} is, however, indirectly increased by the increase in the shear stress, thereby resulting in a net enhancement of $\overline{u^2}$. The distributions of the Reynolds stresses are generally in accordance with these expectations. However, compared with the case without rotation, $\overline{u^2}$ increases by roughly 50 % up to $Ro = 0.10$ and then apparently levels off until a distinct drop in $\overline{u^2}$ is observed for $Ro = 0.50$. This anomalous restabilization is most likely associated with the growth of the irrotational zone where $dU/dy \approx 2\Omega$, which penetrates far into the pressure side at high rotation rates. In this region of neutral stability ($S \approx -1$), the total production of $\overline{u^2}$, i.e. $P_{11} + G_{11} = (1+S)P_{11}$, vanishes. The suppression of $\overline{u^2}$ and the augmentation of $\overline{v^2}$ eventually make the otherwise positive rotational generation term $G_{12} = -2\Omega(\overline{u^2} - \overline{v^2})$ change sign. For the highest rotation rate, $Ro = 0.50$, $\overline{v^2}$ exceeds $\overline{u^2}$ in the range $-0.43 \lesssim y \lesssim 0.83$, i.e. over 63 % of the channel cross-section. This reversal of the conventional stress anisotropy, which renders G_{12} negative rather than positive, is suspected of being responsible for the observed saturation of the increase of $u_{\tau p}$ in figure 6. It is also interesting to notice that the shift of the linear part of the $\overline{uv}$-profiles with increasing Ro simply depends on the increasing asymmetry of the wall shear stresses (cf. (10)).

The fractional contributions to the Reynolds shear stress are shown in figure 8 as a function of y^+. In this quadrant analysis four different categories which contribute to $\overline{uv}$ are classified according to the signs of the velocity fluctuations u and v, where $v > 0$ signifies motion away from the wall. Without rotation the dominating contribution to the shear stress comes from fourth-quadrant or sweep events ($u > 0$ and $v < 0$, i.e. inrush of high-speed fluid) in the near-wall region and from second-quadrant events ($u < 0$ and $v > 0$, i.e. ejections of low-speed fluid) further away from the wall. Contributions from first- and third-quadrant events are generally lower. These characteristics are in agreement with the DNS results of Kim *et al.* (1987). Results for the rotating channel at $Ro = 0.15$ are also presented in figure 8. It is interesting to observe that the general trends of the non-rotating case in figure 8(*a*) are retained on the pressure side shown in figure 8(*b*). The relative contribution from fourth-quadrant events is, however, somewhat reduced. The location of the crossing point, where contributions from ejection and sweep events are equal, is therefore shifted towards the wall (from $y^+ \approx 17$ at $Ro = 0$ to $y^+ \approx 13$ at $Ro = 0.15$). Near the suction side, on the other hand, figure 8(*c*) reveals an anomalous partition of the contributions to $\overline{uv}$. While second- and third-quadrant events are practically negligible near the wall ($y^+ \lesssim 10$), the sweep event appears to be the dominating mechanism for shear stress production. However, the fluid elements approaching the wall during sweep events apparently bounce back while retaining their excessive streamwise momentum. Such first-quadrant bouncing events are outweighing about 50 % of the contribution to $\overline{uv}$ originating from the fourth quadrant.
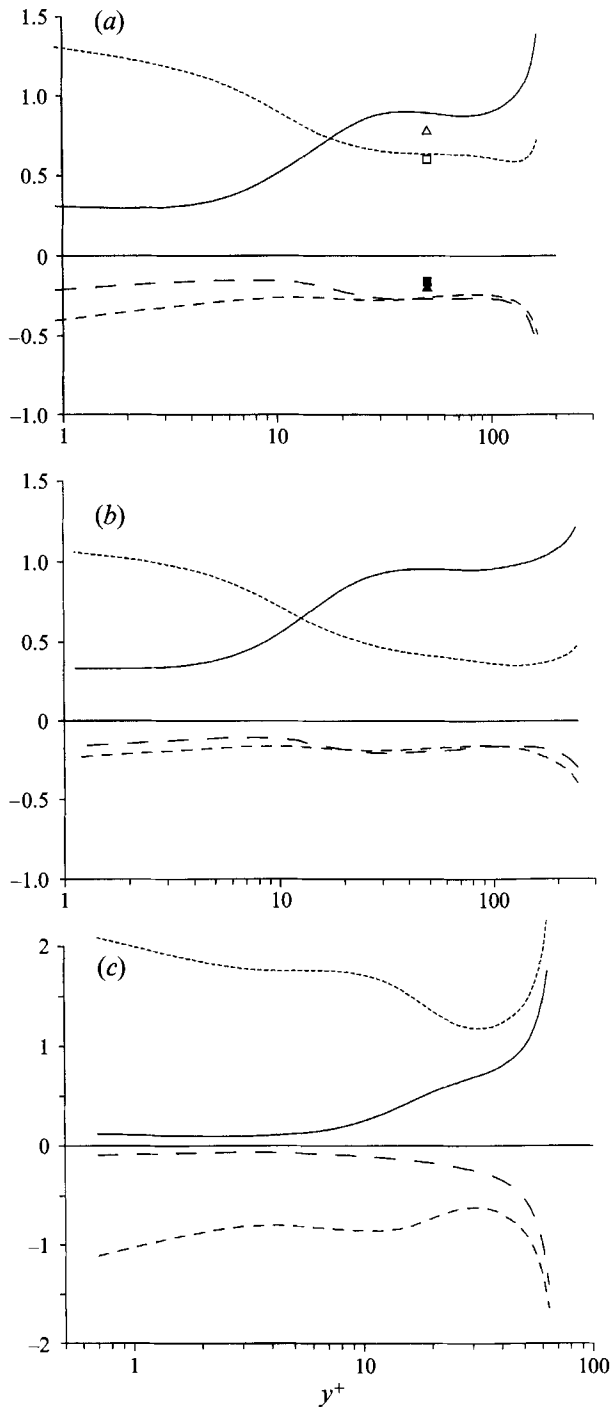
FIGURE 8. Normalized contributions to the Reynolds shear stress from each quadrant: ─────, first; ─────, second; ─────, third; ─────, fourth quadrant. (*a*) $Ro = 0$; symbols denote the experimental data of Alfredsson & Johansson (1984): ▲, first; △, second; ■, third; □, fourth quadrant. (*b*) Pressure side, $Ro = 0.15$. (*c*) Suction side, $Ro = 0.15$.
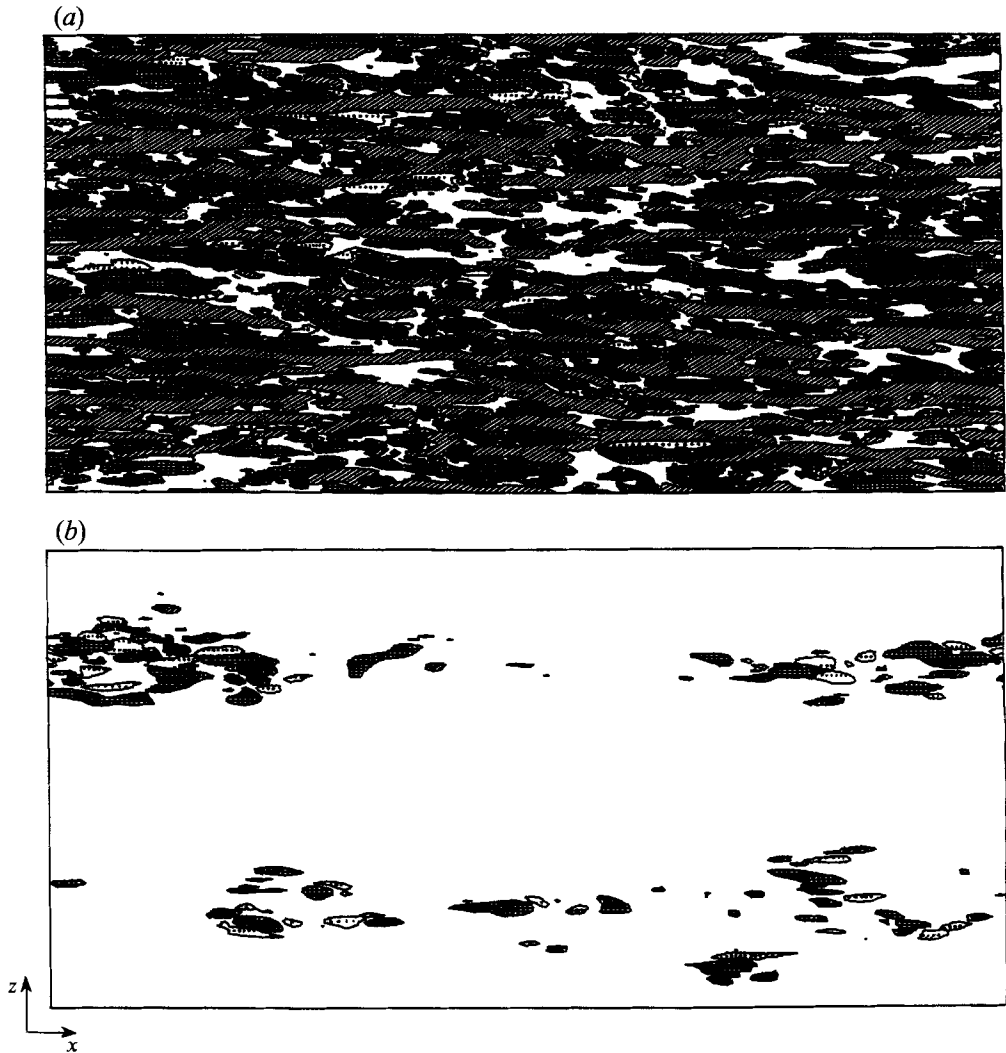
(a)

(b)

FIGURE 9. Instantaneous distribution of Reynolds shear stress in an (x, z)-plane for $Ro = 0.15$; v is defined positive away from the nearest wall. Dotted: $u > 0$, $v > 0$; striped: $u < 0$, $v > 0$; filled: $u < 0$, $v < 0$; cross-hatched: $u > 0$, $v < 0$. (a) Pressure side, $y^+ = 12$; (b) suction side, $y^+ = 8$.

Instantaneous diagrams of fairly intense events, $|uv| > 0.25u_\tau^2$, are presented in figure 9. The two (x, z)-planes considered are positioned at a distance $\Delta y = 0.05$ from the nearest wall, i.e. at about $y^+ \approx 10$. These diagrams highlight the significant difference in turbulence activity between the pressure and suction sides. The relative contributions from the four different patterns, which represent the four quadrants in the uv-plane, are consistent with the averaged contributions in figure 8. The instantaneous picture of the pressure side is dominated by elongated, streaky structures representing sweeps (cross-hatched) and ejections (striped), whereas first- and third-quadrant events are much more sparse and spotty and contribute only marginally to the shear stress $\overline{uv}$. On the suction side, on the other hand, the events above the threshold are scarce and mainly from the first (dotted) and fourth (cross-hatched) quadrants. The intense events on the suction side are also much more spotty than the streaky structures on the pressure side.
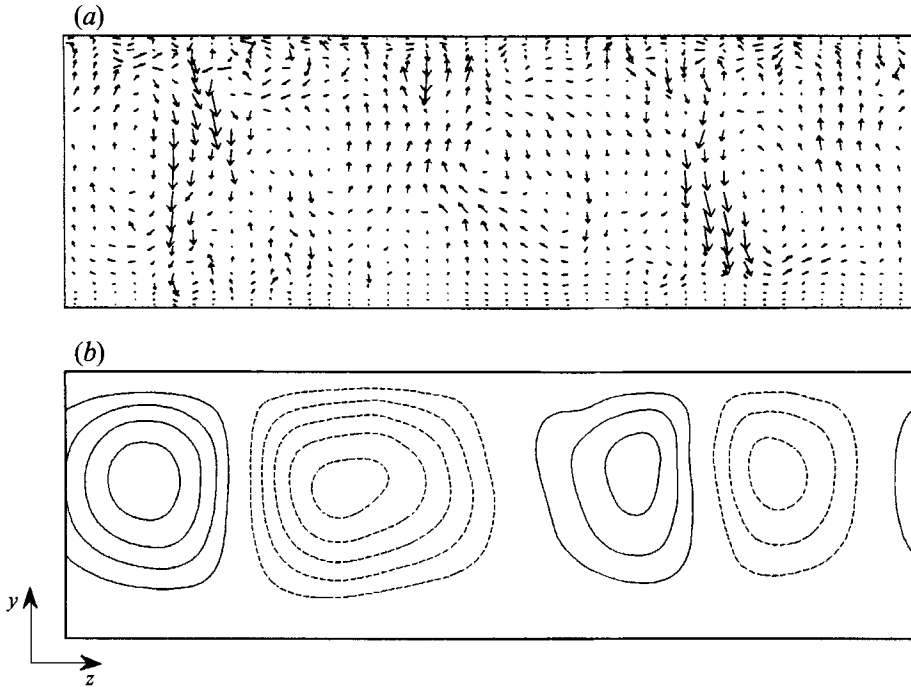
(a)

(b)

FIGURE 10. (a) Instantaneous velocity vectors in a (y, z)-plane at $x = 2\pi$, $Ro = 0.15$; the plotted vectors represent averages over 18 computational cells. (b) Secondary flow streamlines in the (y, z)-plane averaged over $5.6h/u_\tau$, $Ro = 0.15$. Solid and broken lines denote clockwise and counter-clockwise motion, respectively. The pressure side is at the top of the figures.

4.2. *Taylor–Görtler vortices*

The illuminating flow visualizations of Johnston *et al.* (1972) revealed a spanwise array of longitudinal roll cells, which were interpreted as Taylor–Görtler vortices analogous to those arising from the centrifugal instability mechanism associated with streamline curvature. The large-scale vortical structures observed experimentally by Johnston *et al.* were also detected in the large-eddy simulations of Kim (1983) and Miyake & Kajishima (1986 a, b). A cross-sectional view of the directly simulated flow field at $Ro = 0.15$ is shown in figure 10(a). The instantaneous velocity vectors have been projected into the (y, z)-plane midway between the periodic boundaries at $x = 0$ and $x = 4\pi h$. While numerous smaller whirls are observed adjacent to the pressure (top) surface, the motion near the suction (bottom) side seems relatively calm. Two large-scale streams from the pressure to the suction side can also be identified in figure 10(a).

In order to isolate any persistent large-scale flow structures from the underlying turbulence, the instantaneous velocity field is averaged in the streamwise direction and in time. The secondary-flow components $\tilde{v}$ and $\tilde{w}$ that survive the averaging may remain functions of y and z. After averaging over 5.6 letots (h/u_τ), fairly smooth secondary-flow streamlines are obtained (figure 10 b). The depicted streamlines show that two pairs of counter-rotating vortices fill most of the cross-section, although being shifted slightly towards the pressure side. Flow away from the pressure side occurs between the positive and negative member of each vortex pair, whereas the flow between the pairs is directed towards the pressure surface. The density of the streamlines indicates that the flow away from the pressure side is relatively strong compared to the return flow. This fairly intense flow convects low-speed fluid from the

pressure side and out into the core region. It is interesting to notice that the spanwise positions of the two streams across the channel coincide with the locations of the two streamwise bands of high turbulent activity in figure 9(b). The turbulence near the suction side is therefore associated with the presence of the counter-rotating vortices, and the anomalous partition of the fractional contributions of stress-generating events (figure 8c) can thereby be explained.

Although the streamwise vortices are free to move in the spanwise direction, no such drifting of the vortex pattern in figure 10(b) could be observed during the sampling period. It can therefore be concluded that the timescale of spanwise drift, if any, is longer than $5.6h/u_r$. Interestingly, no persistent vortex or roll-cell pattern was observed either in the laboratory by Johnston *et al.* (1972) or in the computer simulations by Kim (1983) and Miyake & Kajishima (1986a, b). Johnston *et al.* (1972) never observed any truly steady cell pattern, but the time period over which a given pattern persisted was long relative to the turbulence timescales. Similarly, Miyake & Kajishima (1986b) found that 'a large scale eddy does not seem to exist stably'. Bradshaw (1973), in his review of effects of streamline curvature, suggests that the influences of upstream disturbances and lateral boundaries may affect the formation of longitudinal vortices and constrain the vortex pattern. Evidently, it is less likely that persistent vortices will form in a laboratory apparatus than in a numerically simulated flow field. In the latter case any streamwise vorticity leaving the calculation domain is fed back by means of the periodic boundary conditions, thereby favouring the formation of roll cells. The use of periodic boundary conditions in the computer simulation can therefore be considered to have an effect analogous to purposely or incidentally introduced upstream non-uniformities. In the simulations, however, nothing prevents the roll cells from spanwise wandering. Since the number of vortex pairs must be an integer N, the aspect ratio of the computational domain does affect the preferred wavelength of the vortices. Assuming that the vortices appear as near-circular roll cells occupying the entire cross-section, the number of pairs can be estimated as

$$N = \text{int} \left(\tfrac{1}{2} W/H \right), \tag{19}$$

where $W = 2\pi h$ and $H = 2h$ are the width and height of the cross-section, respectively. It is likely that an unfavourable aspect ratio may prevent the formation of persistent vortices, and it can be conjectured that this is a more prominent feature of low-aspect-ratio computer simulations than of the higher aspect-ratio laboratory channels. It is therefore interesting to notice that Moser & Moin (1987) observed a single persistent vortex pair, which filled the entire cross-section (aspect ratio $W/H = \tfrac{4}{3}\pi h/2h \approx 2.09$) of their mildly curved channel. Miyake & Kajishima (1986b), on the other hand, chose an aspect ratio $W/H = 1.2$ and inevitably failed to generate a persistent vortex pair in their large-eddy simulation.

The conjectural relation (19) is inherently based on the assumption that the scale of the roll cells (i.e. their diameter) is H. The flow visualizations of Johnston *et al.* (1972) showed that the cells on the pressure side 'extend up to, or beyond, the channel centre-plane' and indicated 'that the cells could extend all the way to the turbulent-laminar interface in those cases where total stabilization occurs on the opposite side'. These observations are consistent with the secondary velocity fields depicted in figure 11. Whereas two vortex pairs can be identified for rotation rates up to $Ro = 0.20$, a third pair appears at $Ro = 0.50$. The thickening of the laminarized wall layer near the suction side obviously tends to reduce the effective height of the cross-section, thereby attempting to increase the number of vortex pairs according to (19). The observation that the scale of the vortices tends to diminish with increasing Ro contrasts with an
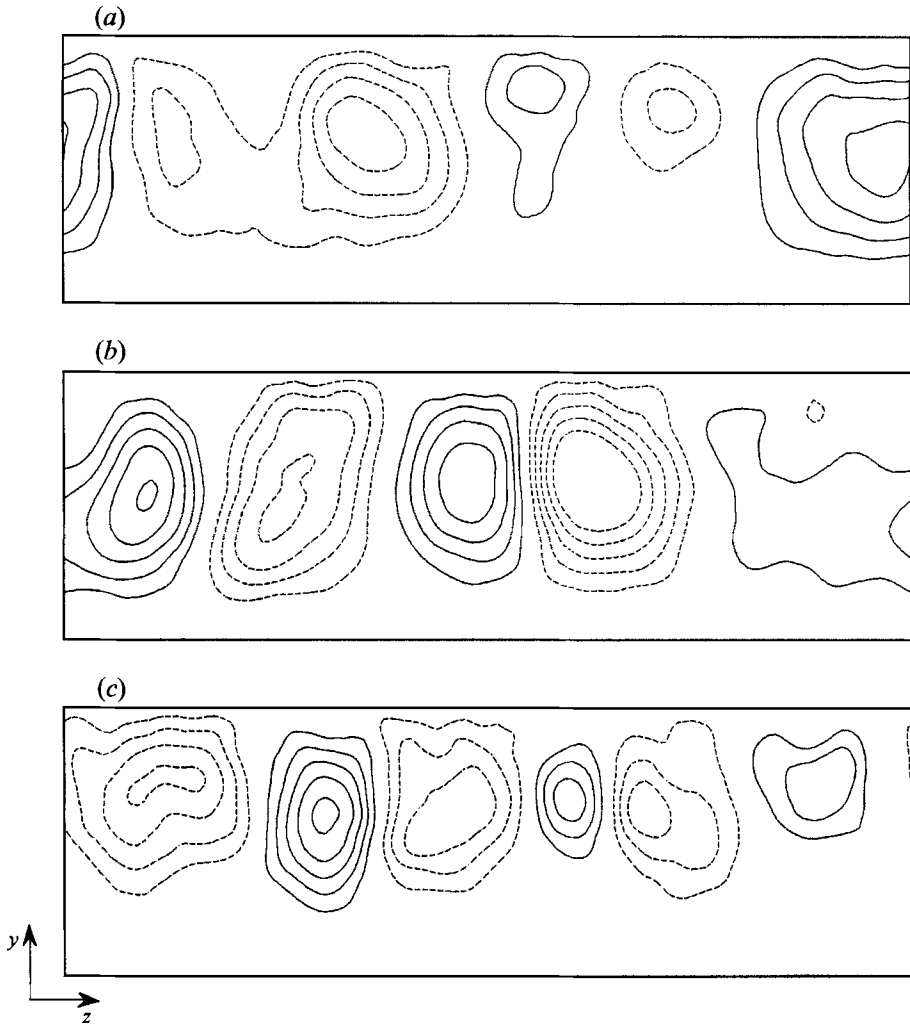
FIGURE 11. Secondary flow streamlines in the (y, z)-plane averaged over $0.4h/u_\tau$. Legend as in figure 10(b). (a) $Ro = 0.10$; (b) $Ro = 0.20$; (c) $Ro = 0.50$.

assumption that the vortices are confined to the destabilized region where $-1 < S < 0$.

It should be pointed out that the secondary flow fields displayed in figure 11 are averaged over significantly shorter (typically only 10%) time spans than the streamlines for $Ro = 0.15$ shown in figure 10(b). Although the locations of the vortices for $Ro = 0.10$ and 0.20 remained unchanged over longer time intervals, their shape, size and strength were gradually changing. Further sampling would accordingly tend to blur the vortex patterns. At the highest rotation rate ($Ro = 0.50$) some vortices were drifting in the lateral directions, and some vortices merged while other disappeared and new ones were created. It can therefore be concluded that the chosen spanwise width of the calculation domain seems to perfectly match the preferred scale of the streamwise vortices at the particular rotation number 0.15 (so as to allow an even number of steady counter-rotating vortices). The corresponding mismatch at the other rotation rates prohibits the formation of a persistent vortex pattern.
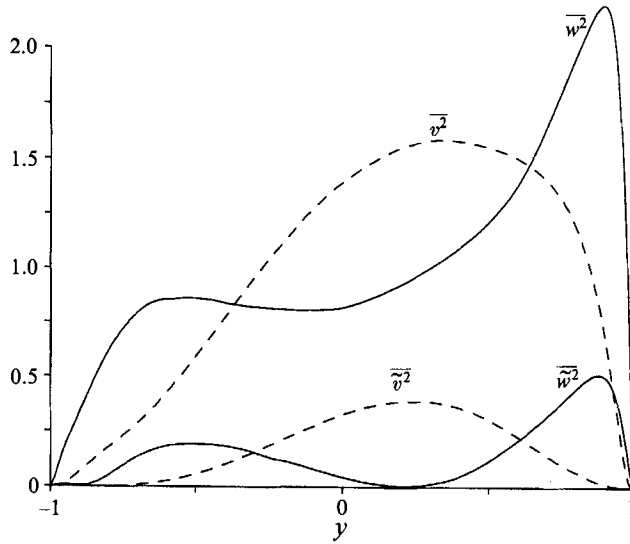
FIGURE 12. Contributions from the Taylor–Görtler vortices to the Reynolds stress components (lower curves) compared with the overall Reynolds stress components (upper curves), $Ro = 0.15$: ––––, v; ——, w.

Obviously, the vortical flow structures do contribute to the computed statistics, for example the Reynolds stress components presented in figure 7. However, the instantaneous velocity components v and w in the (y, z)-plane can be decomposed into contributions from the Taylor–Görtler vortices and real turbulent fluctuations, i.e.

$$v = \tilde{v} + v', \quad w = \tilde{w} + w', \qquad (20\,a, b)$$

where the tilde identifies averages obtained by sampling in the streamwise direction and time. The corresponding Reynolds stresses can now be expressed as

$$\overline{v^2} = \overline{(\tilde{v} + v')^2} = \overline{\tilde{v}^2} + \overline{(v')^2}, \qquad (21\,a)$$

$$\overline{w^2} = \overline{(\tilde{w} + w')^2} = \overline{\tilde{w}^2} + \overline{(w')^2}, \qquad (21\,b)$$

where the overbar indicates conventional averages over homogeneous planes and in time. This decomposition makes sense only in situations where the vortices are persistent structures, and the first term on the right-hand sides of (21) then represents the contribution from the vortices to the Reynolds stresses, whereas the last term accounts for the true turbulence. The profiles of $\overline{\tilde{v}^2}$ and $\overline{\tilde{w}^2}$ in figure 12 indicate that the Taylor–Görtler vortices contribute roughly 25 % of the kinetic energy associated with motions in the cross-sectional plane. The characteristic shapes of the curves in figure 12 also reflect the vortical motions, namely that the flow midway between vortex centres is directed normal to the walls, whereas spanwise motions are dominating near the walls.

4.3. *Two-point correlations*

Single-time two-point velocity correlations $\overline{u_i(x)\,u_j(x+r)}$ were calculated by averaging in time and over planes parallel with the walls. The computed statistics are conventionally normalized by the corresponding one-point correlation $\overline{u_i u_j}$ and expressed in terms of an autocorrelation coefficient, i.e.

$$R_{ij}(y; r) \equiv \overline{u_i(x)\,u_j(x+r)} / \overline{u_i(x)\,u_j(x)}. \qquad (22)$$
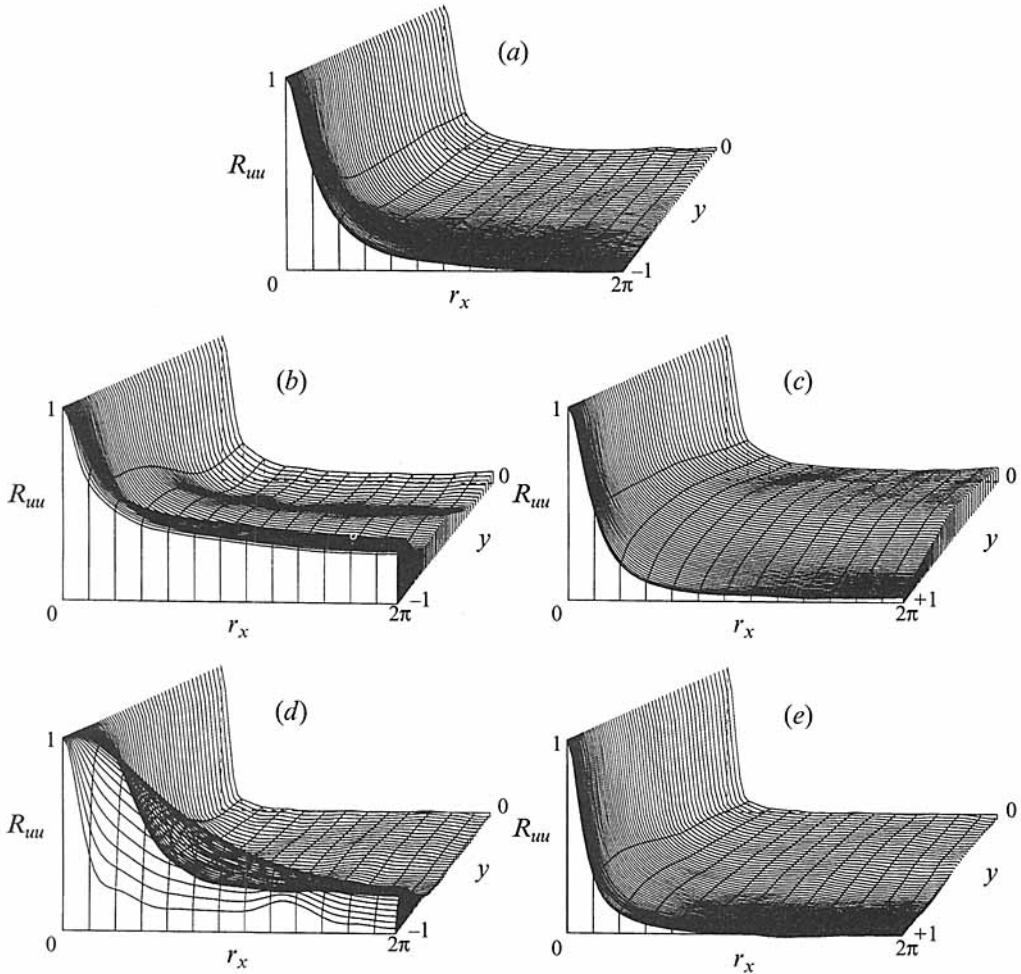
FIGURE 13. Streamwise two-point correlations of u. (*a*) $Ro = 0$; (*b*) $Ro = 0.15$ suction side; (*c*) $Ro = 0.15$ pressure side ; (*d*) $Ro = 0.50$ suction side; (*e*) $Ro = 0.50$ pressure side.

Here, the adopted averaging procedure makes the correlations depend only on the displacement vector r and the y-location. Correlations of the streamwise velocity u at points separated in the streamwise direction are shown in figure 13 for every grid point between the wall and the centre of the channel. The higher density of curves in the near-wall region simply reflects the non-uniformity of the computational grid. Without system rotation it can be observed that the extent in the streamwise direction of appreciable values of R_{uu} is larger near the wall than in the core region. This indication of the elongated wall-layer structures is in accordance with other direct numerical simulations, e.g. Kim *et al.* (1987). Moreover, in figure 13(*a*) all correlations fall off to zero for large separations r_x. Direct comparisons with the recent laboratory experiments by Kasagi & Nishino (1991) are presented in Andersson & Kristoffersen (1992). When the flow is subject to system rotation, the streamwise lengthscales are gradually reduced on the pressure side and increased on the suction side, a tendency which was also observed in the large-eddy simulations by Miyake & Kajishima (1986*a*). The former effect is associated with a shortening of the wall-layer streaks, whereas the latter can be ascribed to the existence of laminarized regions side-by-side
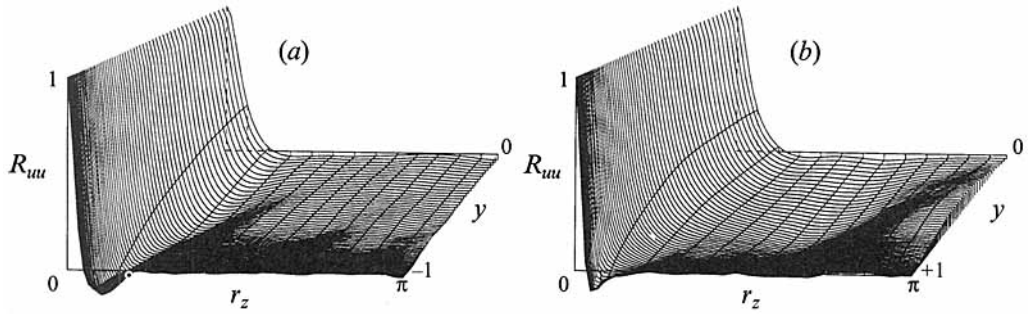
FIGURE 14. Spanwise two-point correlations of u. (a) $Ro = 0$; (b) $Ro = 0.15$ pressure side.

with turbulent areas (see figure 9b and a further discussion in the following section). It is interesting to observe that the correlations between velocity fluctuations at two points away from the pressure side in figure 13(c) do not become negligible at a separation $2\pi h$. These long-lasting correlations at $Ro = 0.15$ mirror the persistent Taylor–Görtler vortices, which extend throughout the calculation domain. At $Ro = 0.50$, on the other hand, the vortical roll cells are wandering as well as having a fairly short lifespan (i.e. shorter than the sampling time). Their presence in the flow field is therefore blurred by the averaging to such an extent that they cannot be discerned in the autocorrelations in figure 13(e).

Spanwise correlation coefficients of the streamwise velocity are presented in figure 14. A notable feature is the appreciable negative correlations in the near-wall region. The separation at which the distinct minimum occurs provides an estimate of the mean separation between high- and low-speed flow (Kim *et al.* 1987). The mean spacing λ between the wall-layer streaks can thus be defined as twice the spanwise separation corresponding to minimum R_{uu}. The topography exhibited by the curves for $Ro = 0$ in figure 14(a) shows that λ increases with the distance from the wall. The same tendency is observed at the pressure side for $Ro = 0.15$ (figure 14b), although not that pronounced. The quantitative comparisons in figure 15 show that the computed mean streak spacing for $Ro = 0$ increases slightly with y^+, i.e. in full agreement with the experimental results of Smith & Metzler (1983) and the DNS data of Kim *et al.* (1987). In the flow subject to weak system rotation ($Ro = 0.01$) the streak spacings are practically identical to the spacing in the non-rotating case. At higher rotation rates, on the other hand, $\lambda^+ \equiv \lambda u_{\tau p}/\nu$ decreases significantly with increasing Ro. Here, it should be emphasized that an even greater reduction of λ has partly been outweighed by the increasing $u_{\tau p}$ (see figure 6). The present findings, which imply higher density of streaks on the pressure side, are consistent with the visual observations made by Kim (1983), namely that 'more streaks are noticeable on the unstable side than on the stable side'. On the other hand, the LES data presented by Miyake & Kajishima (1986a) show that λ remained constant on the pressure side when the rotation number was increased from zero and up to $Ro = 0.165$. Since $u_{\tau p}$ increases with Ro, the constancy of λ implies that λ^+ actually increased with the rotation rate in their LES. Another noticeable feature in figure 14(b) is that the correlations tend to increase for spanwise separations r_z about πh. Since two pairs of persistent Taylor–Görtler vortices are known to fill the width ($W = 2\pi h$) of the calculation domain for $Ro = 0.15$, non-vanishing correlations over this particular distance therefore arise from vortical roll cells with the same sense of rotation.

In figure 16, correlation coefficients of the normal velocity component v at points with spanwise separations r_z are presented. The presence of a distinct minimum of R_{vv}
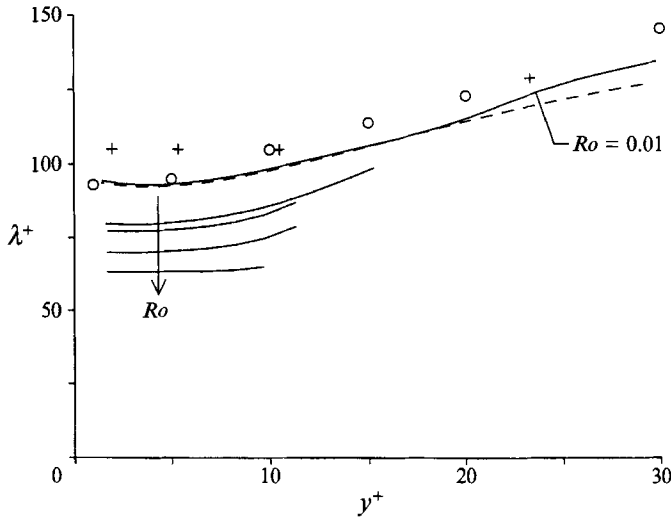
FIGURE 15. Mean spanwise streak spacing $\lambda^+ \equiv \lambda u_{\tau p}/\nu$ near the pressure side for the different rotation rates: ————, $Ro = 0$; ———, $Ro \neq 0$, the case $Ro = 0.10$ is not displayed; ◯, Smith & Metzler (1983); +, Kim *et al.* (1987).
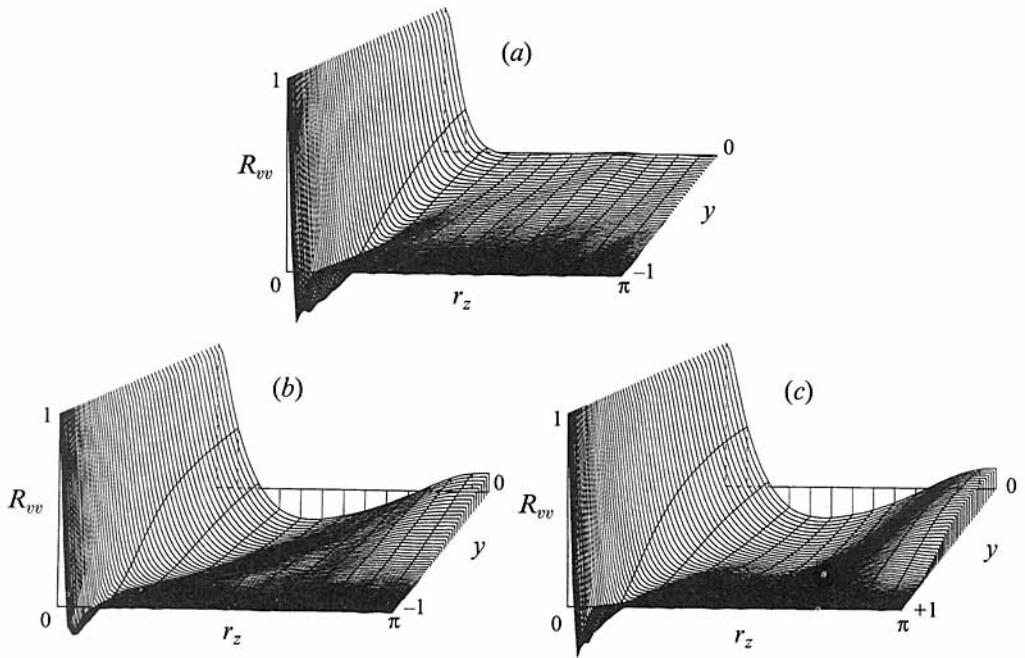

FIGURE 16. Spanwise two-point correlations of v. (*a*) $Ro = 0$; (*b*) $Ro = 0.15$ suction side; (*c*) $Ro = 0.15$ pressure side.

is an accordance with observations by Kim *et al.* (1987) and Moin & Moser (1987), among others. The separation of minimum R_{vv} is interpreted as the mean diameter of the vortical streamwise structures in the innermost wall layer. With system rotation $Ro = 0.15$ imposed, these characteristic minima remain on both sides of the channel. It is noteworthy that the separation r_z corresponding to minimum R_{vv} has been increased by rotation on the suction side, thus indicating a broadening of the streaky structures on that side. The appreciable negative correlations in the core region near
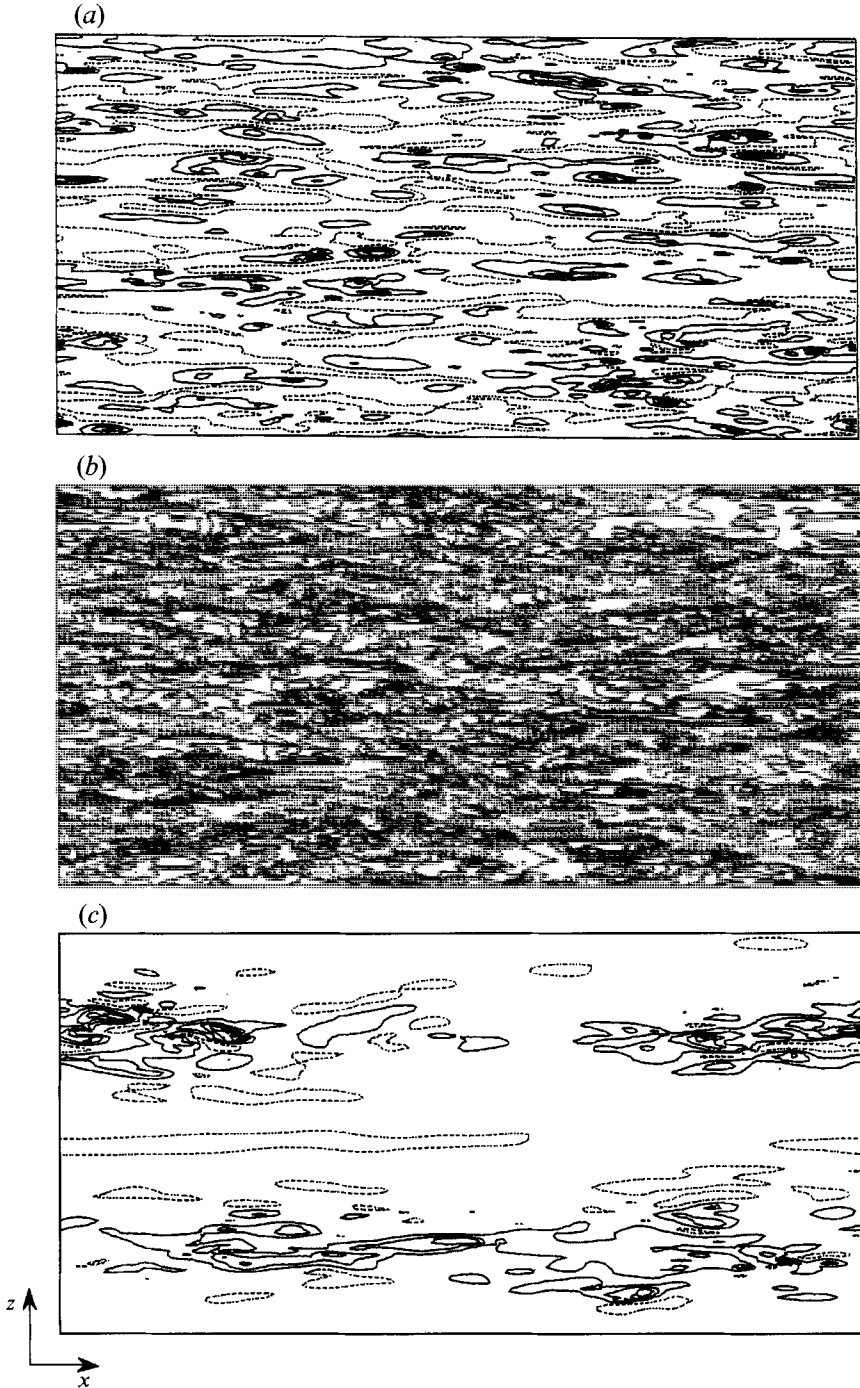
(a)

(b)

(c)

FIGURE 17. Contour plots of instantaneous streamwise velocity fluctuations in the (x, z)-plane at $y^+ = 12$. Broken lines denote negative values. (a) $Ro = 0$; (b) $Ro = 0.15$ pressure side; (c) $Ro = 0.15$ suction side.
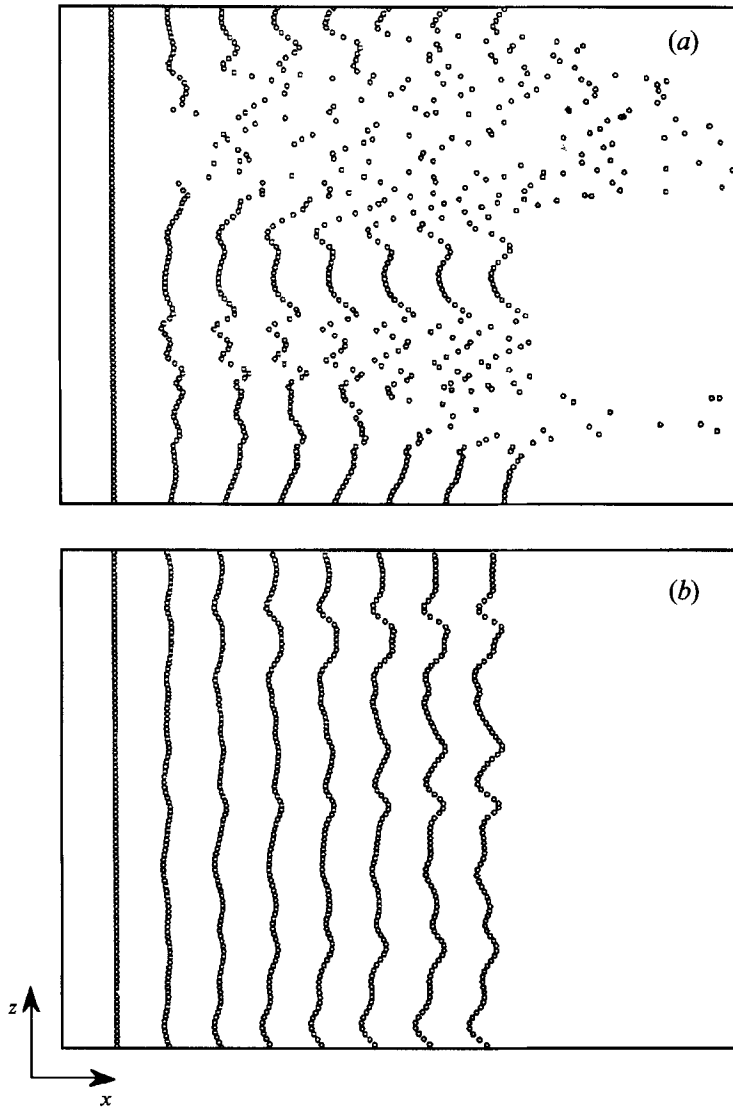
FIGURE 18. Marker particles generated along a line parallel to the z-axis at $y^+ = 1$, suction side. Only $1/10$ of the channel length is shown, and the ratio length/width is not preserved in the figures. (*a*) $Ro = 0.15$; (*b*) $Ro = 0.50$.

$r_z = \frac{1}{2}\pi h$ and the positive correlations near $r_z = \pi h$ is another manifestation of the steady counter-rotating Taylor–Görtler vortices for $Ro = 0.15$ depicted in figure 10 (*b*).

4.4. *Visualizations of flow structures*

In contrast to one-point and two-point statistics that provide quantitative information about the flow field, flow visualization studies are basically of a qualitative nature. Visual observations may nevertheless help to prove or disprove conclusions already drawn from the computed statistics and they may, moreover, reveal crucial information that is lost in the process of averaging. A typical example is the visualization of the streaky flow pattern in the near-wall region depicted in figure 17. The contour plots of the instantaneous streamwise velocity component u in a plane parallel to the wall at
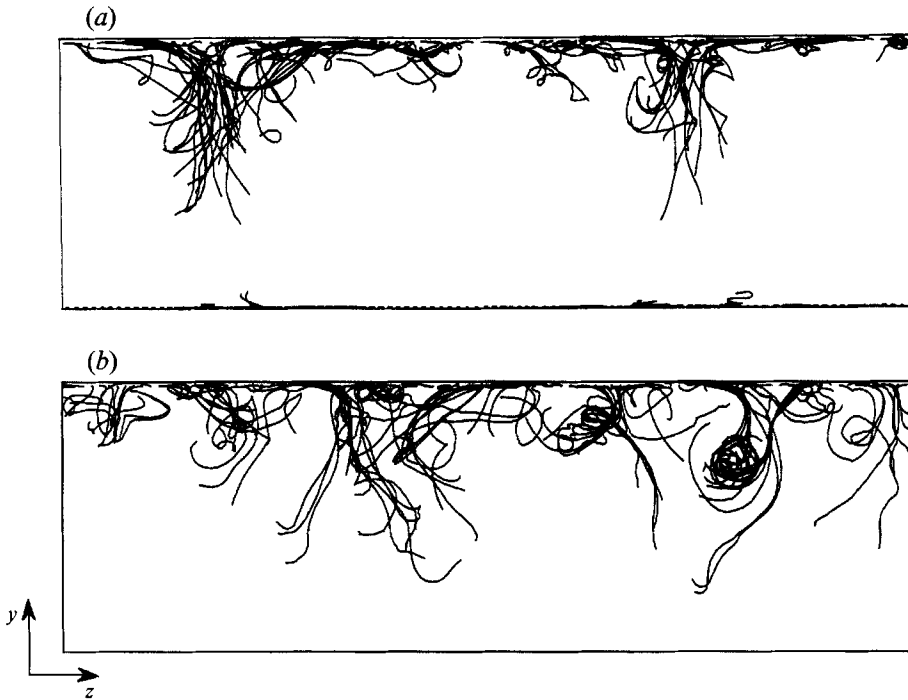
(a)

(b)

FIGURE 19. Paths of marker particles generated along a line parallel to the z-axis at $y^+ = 1$ on both sides, viewed along the x-axis. The top of the figures is the pressure side. (a) $Ro = 0.15$; (b) $Ro = 0.50$.

about $y^+ = 12$ exhibit elongated regions of high- and low-speed motions. The striking effect of system rotation is to increase the number and the intensity of the streaks along the pressure side (figure 17b), while the number of streaks are reduced on the suction side (figure 17c). Interestingly, the elongated streaks on the stabilized side seem to occur only in two streamwise bands which coincide with the impingement zone of the Taylor–Görtler vortices. It is moreover noteworthy that the turbulence intensity within these streaks is comparable with the activity in the non-rotating case. It can therefore be concluded that the reduction in the overall level of $\overline{u^2}$ on the suction side is caused by the occurrence of calm regions in between the more vigorous bands, whereas the increased level of $\overline{u^2}$ on the pressure side is associated with the greater number of evenly distributed, but more intense, streaks.

Hydrogen-bubble timelines, as provided experimentally by Johnston et al. (1972), can be simulated numerically by generating passive particles along a spanwise line. The particles released at $y^+ \approx 1$ are tracked continuously but displayed only at every $0.1 h/u_\tau$, at which another set of particles is generated. The timelines adjacent to the suction side for $Ro = 0.15$, as displayed in figure 18(a), show striking similarities with the picture for $Ro = 0.107$ presented by Johnston et al. (1972, figure 8d). They found that the near-wall layer is only partly turbulent and that 'laminar regions are seen, side-by-side with turbulent spots'. Here, laminar flow was recognized as regions where timelines are parallel to each other. Johnston et al. called this flow regime 'transitional', while fully laminar flow was proclaimed when no turbulent spots were seen for a long period of time. The latter flow condition corresponds to the situation in figure 18(b), where the timelines for $Ro = 0.50$ remain nearly parallel over an appreciable lapse of time.
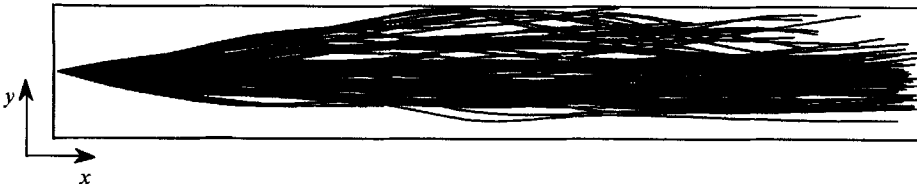
FIGURE 20. Paths of marker particles generated along a line parallel to the z-axis at the channel centre, viewed along the z-axis.

The paths traversed by the particles released during the first discharge in figure 18 are shown in figure 19. The frontal view of the pathlines demonstrate that the particles originating from the pressure side ($y^+ \approx 1$) tend to move away from the wall in two distinct streams associated with the vortical roll cells depicted in figure 10(b). Apparently, the particles are convected into the core region by the Taylor–Görtler vortices while being dispersed by the turbulent motions. On the other hand, the paths of the particles released adjacent to the suction side can scarcely be discerned. The particles in the calmer region are convected in the downstream direction and exposed to transverse excursions only in the regions where the streams arising from the vortical cells approach the suction side. The unsteadiness of the Taylor–Görtler vortices at $Ro = 0.50$ makes the cell structure unrecognizable in figure 18(b). In spite of the vigorous motion in the core and at the pressure side, the pathlines adjacent to the suction side are practically unaffected. Figure 20 shows a side view of pathlines of particles released from an upstream line parallel to the z-axis and positioned midway between the walls. The particles are observed to spread quite rapidly over most of the cross-section, but no particles are dispersed into the calm layer at the suction side. This is in accordance with photographs and motion pictures by Johnston *et al.* (1972), from which they observed 'a remarkably sharp line of demarcation or "interface" between stabilized and destabilized fluid'.

5. Concluding remarks

The direct numerical simulation of fully developed low-Reynolds-number turbulent flow in a non-rotating channel compared favourably with the highly accurate reference simulation of Kim *et al.* (1987) as well as with the recent measurements of Nishino & Kasagi (1989) using particle tracking velocimetry. When the channel was set into spanwise rotation the crucial influence of the Coriolis force was examined for six different rotation numbers, ranging from weak ($Ro = 0.01$) to strong rotation ($Ro = 0.50$). Among the many effects of rotation observed the following are quite significant:

(i) The profiles of the turbulence statistics are only slightly affected at the lowest rotation rate ($Ro = 0.01$). The effects observed along the stabilized suction side and the destabilized pressure side are nearly opposite when compared to each other.

(ii) The turbulent Reynolds stresses decreased gradually with increasing Ro near the suction side of the channel, while the turbulence intensities in the normal and spanwise directions increased monotonically at the pressure side. The streamwise intensity and the Reynolds shear stress component, on the other hand, were also increased at the pressure side with moderate rotation imposed, but $\overline{uu}$, in particular, was suppressed (restabilized) at the highest rotation rates considered. These observations could all be explained in terms of the joint action of the mean shear and rotational production terms in the Reynolds stress budgets.

(iii) The mean velocity profile became increasingly asymmetric with increasing rotation numbers. A substantial region with slope proportional to 2Ω was established in the centre region, in accordance with the experimental observations of Johnston *et al.* (1972) and Johnston (1973).

(iv) The turbulence along the suction side was quenched at the highest rotation rates. This striking laminarization was visualized by particle tracking techniques and mirrored in the computed two-point correlations. Most strikingly, perhaps, was the vanishing of the Reynolds stresses next to the stabilized wall.

(v) The existence of large-scale Taylor–Görtler-like vortical structures in the rotating flow fields, as observed experimentally by Johnston *et al.* (1972), was confirmed. These vortices are responsible for transportation of highly turbulent fluid from the pressure side out into the middle of the channel, thereby leading to an enhanced turbulence level midway between the two planes. The number of vortex pairs seems to increase with *Ro*, and the vortices are also being shifted towards the pressure side. Unfortunately, these vortices are unstable for all rotation numbers considered but 0.15, and we have therefore been unable to separate their contribution to the Reynolds stresses from that of the underlying turbulence.

The numerical experiments reported herein provide supplementary information to the few existing laboratory investigations of fully developed rotating channel flow. The computer-generated data therefore represent a valuable reference, against which new and existing turbulence models can be tested and validated.

REFERENCES

ALFREDSSON, P. H. & JOHANSSON, A. V. 1984 On the detection of turbulence-generating events. *J. Fluid Mech.* **139**, 325–345.

ALFREDSSON, P. H., JOHANSSON, A. V., HARITONIDIS, J. H. & ECKELMANN, H. 1988 The fluctuating wall-shear stress and the velocity field in the viscous sublayer. *Phys. Fluids* **31**, 1026–1033.

ALFREDSSON, P. H. & PERSSON, H. 1989 Instabilities in channel flow with system rotation. *J. Fluid Mech.* **202**, 543–557.

ANDERSSON, H. I. & KRISTOFFERSEN, R. 1992 Statistics of numerically generated turbulence. *Acta Appl. Math.* **26**, 293–314.

ANDERSSON, H. I. & MAZUMDAR, H. P. 1993 Rapid distortion of homogeneous low Reynolds number turbulence by uniform shear and weak rotation. *Eur. J. Mech.* B. *Fluids* **12**, 31–42.

BERTOGLIO, J.-P. 1982 Homogeneous turbulent field within a rotating frame. *AIAA J.* **20**, 1175–1181.

BIDOKHTI, A. A. & TRITTON, D. J. 1992 The structure of a turbulent free shear layer in a rotating fluid. *J. Fluid Mech.* **241**, 469–502.

BRADSHAW, P. 1969 The analogy between streamline curvature and buoyancy in turbulent shear flow. *J. Fluid Mech.* **36**, 177–191.

BRADSHAW, P. 1973 Effects of streamline curvature on turbulent flow. *AGARDograph* 169.

CAMBON, C., BENOIT, J. P., SHAO, L. & JACQUIN, L. 1993 Stability analysis and direct simulation of rotating turbulence with organized eddies. In *Some Applied Problems in Fluid Mechanics* (ed. H. P. Mazumdar), pp. 125–153. Indian Statistical Institute.

CAMBON, C. & JACQUIN, L. 1989 Spectral approach to non-isotropic turbulence subjected to rotation. *J. Fluid Mech.* **202**, 295–317.

CAMBON, C., TEISSEDRE, C. & JEANDEL, D. 1985 Etude d'effets couplés de déformation et de rotation sur une turbulence homogène. *J. Méc. Théor. Appl.* **4**, 629–657.

COUSTEIX, J. & AUPOIX, B. 1981 Modélisation des équations aux tensions de Reynolds dans un repere en rotation. *La Recherche Aérospatiale* No. 1981-4, pp. 275–285.

DEAN, R. B. 1978 Reynolds number dependence of skin friction and other bulk flow variables in two-dimensional rectangular duct flow. *Trans. ASME* I: *J. Fluids Engng* **100**, 215–223.

DEARDORFF, J. W. 1970 A numerical study of three-dimensional turbulent channel flow at large Reynolds numbers. *J. Fluid Mech.* **41**, 453–480.

ECKELMANN, H. 1974 The structure of the viscous sublayer and the adjacent wall region in a turbulent channel flow. *J. Fluid Mech.* **65**, 439–459.

GALPERIN, B. & MELLOR, G. L. 1991 The effects of streamline curvature and spanwise rotation on near-surface, turbulent boundary layers. *Z. Angew. Math. Phys.* **42**, 565–583.

GAVRILAKIS, S., TSAI, H. M., VOKE, P. R. & LESLIE, D. C. 1986 Large-eddy simulation of low Reynolds number channel flow by spectral and finite difference methods. In *Direct and Large Eddy Simulation of Turbulence* (ed. U. Schumann & R. Friedrich). Notes on Numerical Fluid Mechanics, vol. 15, pp. 105–118. Vieweg.

HILL, P. G. & MOON, I. M. 1962 Effects of Coriolis on the turbulent boundary layer in rotating fluid machines. *MIT Gas Turbine Lab. Rep.* 69.

HOPFINGER, E. J. 1989 Turbulence and vortices in rotating fluids. In *Theoretical and Applied Mechanics* (ed. P. Germain, M. Piau & D. Caillerie), pp. 117–138. Elsevier.

HOPFINGER, E. J. & LINDEN, P. F. 1990 The effect of background rotation on fluid motions: a report on Euromech 245. *J. Fluid Mech.* **211**, 417–435.

HOWARD, J. H. G., PATANKAR, S. V. & BORDYNUIK, R. M. 1980 Flow prediction in rotating ducts using Coriolis-modified turbulence models. *Trans. ASME* I: *J. Fluids Engng* **102**, 456–461.

IBAL, G. 1990 Adverse pressure gradient and separating turbulent boundary layer flows with system rotation. PhD thesis, University of Melbourne.

JOHNSTON, J. P. 1973 The suppression of shear layer turbulence in rotating systems. *Trans. ASME* I: *J. Fluids Engng* **95**, 229–236.

JOHNSTON, J. P. & EIDE, S. A. 1976 Turbulent boundary layers on centrifugal compressor blades: prediction of the effects of surface curvature and rotation. *Trans. ASME* I: *J. Fluids Engng* **98**, 374–381.

JOHNSTON, J. P., HALLEEN, R. M. & LEZIUS, D. K. 1972 Effects of spanwise rotation on the structure of two-dimensional fully developed turbulent channel flow. *J. Fluid Mech.* **56**, 533–557.

KARLSSON, R. I. 1993 Near-wall measurements of turbulence structure in boundary layers and wall jets. In *Near-Wall Turbulent Flows* (ed. R. M. C. So, C. G. Speziale & B. E. Launder), pp. 423–432. Elsevier.

KARLSSON, R. I. & JOHANSSON, T. G. 1988 LDV measurements of higher order moments of velocity fluctuations in a turbulent boundary layer. In *Laser Anemometry in Fluid Mechanics III* (ed. R. J. Adrian, T. Asanuma, D. F. G. Durao, F. Durst & J. H. Whitelaw), pp. 273–289. Ladoan-Instituto Superior Tecnico.

KASAGI, N. & HIRATA, M. 1975 Transport phenomena in near-wall region of turbulent boundary layer around a rotating cylinder. *ASME Winter Annual Meeting, Houston, Paper* 75-WA/HT-58.

KASAGI, N. & NISHINO, K. 1991 Probing turbulence with three-dimensional particle-tracking velocimetry. *Exp. Thermal Fluid Sci.* **4**, 601–612.

KIKUYAMA, K., NISHIBORI, K., MURAKAMI, M. & HARA, S. 1987 Effects of system rotation upon turbulent boundary layer on a concave surface. In *Proc. 6th Symp. on Turbulent Shear Flows, Toulouse*, pp. 1.4.1-6.

KIM, J. 1983 The effect of rotation on turbulence structure. In *Proc. 4th Symp. on Turbulent Shear Flows, Karlsruhe*, pp. 6.14–6.19.

KIM, J., MOIN, P. & MOSER, R. 1987 Turbulence statistics in fully developed channel flow at low Reynolds number. *J. Fluid Mech.* **177**, 133–166.

KOYAMA, H., MASUDA, S., ARIGA, I. & WATANABE, I. 1979 Stabilizing and destabilizing effects of Coriolis force on two-dimensional laminar and turbulent boundary layers. *Trans. ASME* A: *J. Engng Power* **101**, 25–31.

KOYAMA, H. S. & OHUCHI, M. 1985 Effects of Coriolis force on boundary layer development. In *Proc. 5th Symp. on Turbulent Shear Flows, Ithaca*, pp. 21.19–21.24.

KREPLIN, H.-P. & ECKELMANN, M. 1979 Behavior of the three fluctuating velocity components in the wall region of a turbulent channel flow. *Phys. Fluids* **22**, 1233–1239.

KRISTOFFERSEN, R. & ANDERSSON, H. I. 1991 Numerical transition to turbulence in plane Poiseuille flow. In *Numerical Methods in Laminar and Turbulent Flow* (ed. C. Taylor, J. H. Chin & G. M. Homsy), vol. 7, pp. 222–232. Pineridge.

KRISTOFFERSEN, R., NILSEN, P. J. & ANDERSSON, H. I. 1990 Validation of Reynolds stress closures for rotating channel flows by means of direct numerical simulations. In *Engineering Turbulence Modelling and Experiments* (ed. W. Rodi & E. N. Ganic), pp. 55–64. Elsevier.

LAUNDER, B. E. 1889a Second-moment closure: present... and future? *Intl J. Heat Fluid Flow* **10**, 282–300.

LAUNDER, B. E. 1989b Second-moment closure and its use in modelling turbulent industrial flows. *Intl J. Num. Meth. Fluids* **9**, 963–985.

LAUNDER, B. E. & TSELEPIDAKIS, D. P. 1993 Application of a new second-moment closure to turbulent channel flow rotating in orthogonal mode. *Intl. J. Heat Fluid Flow* (to appear).

LAUNDER, B. E., TSELEPIDAKIS, D. P. & YOUNIS, B. A. 1987 A second-moment closure study of rotating channel flow. *J. Fluid Mech.* **183**, 63–75.

MASUDA, S., OKAMAE, K. & ARIGA, I. 1985 Transition of boundary layer on rotating flat plate. In *Laminar–Turbulent Transition* (ed. V. V. Kozlov), pp. 699–704. Springer.

MIYAKE, Y. & KAJISHIMA, T. 1986a Numerical simulation of the effects of Coriolis force on the structure of turbulence. Global effects. *Bull. JSME* **29**, 3341–3346.

MIYAKE, Y. & KAJISHIMA, T. 1986b Numerical simulation of the effects of Coriolis force on the structure of turbulence. Structure of turbulence. *Bull. JSME* **29**, 3347–3351.

MOIN, P. & KIM, J. 1982 Numerical investigation of turbulent channel flow. *J. Fluid Mech.* **118**, 341–377.

MOON, I. M. 1964 Effects of Coriolis forces on the turbulent boundary layer in rotating fluid machines. *MIT Gas Turbine Lab. Rep.* 74.

MOORE, J. 1967 Effect of Coriolis on turbulent flow in rotating rectangular channels. *MIT Gas Turbine Lab. Rep.* 89.

MOSER, R. D. & MOIN, P. 1987 The effect of curvature in wall-bounded turbulent flows. *J. Fluid Mech.* **175**, 479–510.

NILSEN, P. J. & ANDERSSON, H. I. 1990a Reynolds stress modelling of developing flow in a rotating channel. In *Proc. 4th Intl Symp. on Refined Flow Modelling and Turbulence Measurements, Wuhan* (ed. Z. Liang, C. J. Chen & S. Cai), pp. 54–61. IAHR.

NILSEN, P. J. & ANDERSSON, H. I. 1990b Rotational effects on sudden expansion flows. In *Engineering Turbulence Modelling and Experiments* (ed. W. Rodi & E. N. Ganic), pp. 65–72. Elsevier.

NILSEN, P. J. & ANDERSSON, H. I. 1993 Modelling the effects of solid-body rotation on turbulent mixing-layers. In *Engineering Turbulence Modelling and Experiments 2* (ed. W. Rodi & F. Martelli), pp. 83–92. Elsevier.

NISHINO, K. & KASAGI, N. 1989 Turbulence statistics measurements in a two-dimensional channel flow using a three-dimensional particle tracking velocimeter. In *Proc. 7th Symp. on Turbulent Shear Flows, Stanford*, pp. 22.1.1–6.

ROTHE, P. H. & JOHNSTON, J. P. 1979 Free shear layer behavior in rotating systems. *Trans. ASME* I: *J. Fluids Engng* **101**, 117–120.

SCHUMANN, U. 1975 Subgrid scale model for finite difference simulations of turbulent flows in plane channels and annuli. *J. Comput. Phys,.* **18**, 376–404.

SHIMA, N. 1993 Prediction of turbulent boundary layers with a second-moment closure: Part II – Effects of streamline curvature and spanwise rotation. *Trans. ASME* I: *J. Fluids Engng* **115**, 64–69.

SMITH, C. R. & METZLER, S. P. 1983 The characteristics of low-speed streaks in the near-wall region of a turbulent boundary layer. *J. Fluid Mech.* **129**, 27–54.

SPEZIALE, C. G. 1982 Numerical study of viscous flow in rotating rectangular ducts. *J. Fluid Mech.* **122**, 251–271.

SPEZIALE, C. G. 1986 The effect of the Earth's rotation on channel flow. *Trans. ASME* E: *J. Appl. Mech.* **53**, 198–202.

SPEZIALE, C. G. & THANGHAM, S. 1983 Numerical study of secondary flows and roll-cell instabilities in rotating channel flow. *J. Fluid Mech.* **130**, 377–395.

TAYLOR, G. I. 1935 Distribution of velocity and temperature between concentric rotating cylinders. *Proc. R. Soc. Lond.* A **151**, 494–512.

THOMAS, T. G. & TAKHAR, H. S. 1988 Frame-invariance of turbulence constitutive relations. *Astrophys. Space Sci.* **141**, 159–168.

TRITTON, D. J. 1978 Turbulence in rotating fluids. In *Rotating Fluids in Geophysics* (ed. P. H. Roberts & A. M. Soward), pp. 105–138. Academic.

TRITTON, D. J. 1985 Experiments on turbulence in geophysical fluid dynamics. In *Turbulence and Predictability in Geophysical Fluid Dynamics and Climate Dynamics* (ed. M. Ghil), pp. 172–192. North-Holland.

TRITTON, D. J. 1992 Stabilization and destabilization of turbulent shear flow in a rotating fluid. *J. Fluid Mech.* **241**, 503–523.

TRITTON, D. J. & DAVIES, P. A. 1981 Instabilities in geophysical fluid dynamics. In *Hydrodynamic Instabilities and the Transition to Turbulence*. Topics in Applied Physics (ed. H. L. Swinney & J. P. Gollub), vol. 45, pp. 229–269. Springer.

WATMUFF, J. H., WITT, H. T. & JOUBERT, P. N. 1985 Developing turbulent boundary layers with system rotation. *J. Fluid Mech.* **157**, 405–448.

WATTENDORF, F. L. 1935 A study of the effect of curvature on fully developed turbulent flow. *Proc. R. Soc. Lond.* A **148**, 565–598.

WITT, H. T. & JOUBERT, P. N. 1985 Effects of rotation on turbulent wakes. In *Proc. 5th Symposium on Turbulent Shear Flows, Ithaca*, pp. 21.25–21.30.